





RESEARCH ARTICLE

A two-dimensional, reach-scale implementation of space-time image velocimetry (STIV) and comparison to particle image velocimetry (PIV)

Carl J. Legleiter¹  | Paul J. Kinzel¹  | Frank L. Engel²  | Lee R. Harrison^{3,4}  | Gregory Hewitt⁵

¹US Geological Survey, Observing Systems Division, Golden, Colorado, USA

²US Geological Survey, Observing Systems Division, San Antonio, Texas, USA

³National Oceanographic and Atmospheric Administration, Southwest Fisheries Science Center, Santa Cruz, California, USA

⁴Earth Research Institute, University of California, Santa Barbara, California, USA

⁵Deep Analytics, LLC, Montpelier, Vermont, USA

Correspondence

Carl Legleiter, US Geological Survey, Observing Systems Division, Golden, CO 80403, USA.

Email: cjl@usgs.gov

Abstract

Image-based algorithms have become a powerful tool for estimating flow velocities in rivers. In this study, we generalize the space-time image velocimetry (STIV) framework for reach-scale application rather than along a cross section. The new algorithm provides information on both the magnitude and orientation of velocity vectors, and we refer to the algorithm as two-dimensional STIV, or 2D-STIV. The workflow involves setting up a grid, using centreline tangent vectors as initial estimates of flow direction, and then extracting space-time images (STIs) along search lines radiating from each grid node. The autocorrelation function is used to infer the inclination of streak lines present in STIs, which represents the advection of water surface features. Information on flow direction is obtained by evaluating various candidate search lines and identifying that which yields the highest velocity. This search can be performed exhaustively or via optimization. We applied the new 2D-STIV algorithm to three test cases, one simulated data set and two natural channels, and compared image-derived velocities to modelled or measured values. We also applied two established particle image velocimetry (PIV) algorithms to the same data sets. 2D-STIV performed as well as the two PIV algorithms for simulated images. For a natural river with distinct water surface features, 2D-STIV was effective for much of the channel but also led to a more patchy, irregular velocity field than the two PIV algorithms. For a site lacking obvious surface features, exhaustive 2D-STIV led to velocity estimates uncorrelated with field data while the optimization-based version produced erratic flow directions. 2D-STIV also required greater image sequence durations, higher frame rates, and generally longer computational run times. Overall, ensemble PIV was the most reliable algorithm.

KEYWORDS

noncontact flow measurement, particle image velocimetry (PIV), space-time image velocimetry (STIV), two-dimensional velocity field, uncrewed aircraft systems (UAS)

1 | INTRODUCTION

Over the past three decades, remote sensing methods have emerged as a powerful tool for quantitative mapping and monitoring of river systems (Carbonneau et al., 2012; Marcus & Fonstad, 2010; Piégay et al., 2020). A prominent aspect of this trend is the broader uptake of image-

based algorithms for estimating flow velocities in river channels (Dal Sasso et al., 2021; Jolley et al., 2021; Strelnikova et al., 2023). Image velocimetry can provide detailed information on complex flow patterns and offers a number of significant advantages relative to conventional field methods. For example, the ability to measure velocities remotely, without placing instruments into the water, is particularly important

when high flows or other hazardous conditions like ice, debris, or contamination of the river make standard techniques like acoustic Doppler current profiling (ADCP) onerous to implement and can place personnel at risk. In addition, image-based algorithms can be used to map flow fields at high spatial resolution and over large areas (Legleiter et al., 2023), including locations that are difficult to access. These efficiencies also open up the possibility of reducing costs and expanding hydrologic monitoring networks into ungaged basins (e.g., Conaway et al., 2019). Another factor facilitating the expansion of image-based river velocimetry is the growing range of platforms from which suitable image data can be acquired. In addition to more established bridge- or bank-mounted cameras (e.g., Muste et al., 2008) and helicopters (Fujita & Hino, 2003), various uncrewed aircraft systems (UAS) are now widely used to collect nadir-viewing river images (e.g., Eltner et al., 2021). Recent studies have also demonstrated the potential to map flow velocities from moving, fixed-wing aircraft (Legleiter et al., 2023) or even satellites (Legleiter & Kinzel, 2021). Although optical images and RGB (red-green-blue) video are the most common data types used for velocity mapping, thermal cameras can also serve this purpose if water surface features expressed as subtle differences in temperature can be detected and tracked (Schweitzer & Cowen, 2021).

In parallel with these advances in data acquisition, a wide variety of algorithms for inferring velocities from image time series have been and continue to be developed. Proven algorithms include particle image velocimetry (PIV; Muste et al., 2008), particle tracking velocimetry (PTV; Eltner et al., 2020), optical tracking velocimetry (Tauro et al., 2018), space-time image velocimetry (STIV; Fujita et al., 2007), and numerous variants of optical flow (e.g., Hutley et al., 2023). These algorithms are accessible to a growing community of end users through various software tools (Jolley et al., 2021), such as RIVeR (Patalano et al., 2017), FlowVeloTool (Eltner et al., 2020), KLT-IV (Perks, 2020), Hydro-STIV (Watanabe et al., 2021), and TRIVIA (Legleiter & Kinzel, 2023b). The availability of these programs allows for the use of image velocimetry in a wide range of applications, including noncontact streamflow (i.e., discharge) measurement (Peña-Haro et al., 2021) and efforts to link hydraulic heterogeneity to habitat suitability for aquatic organisms (Strelnikova et al., 2020). As these tools begin to be incorporated into reach-scale monitoring programs (e.g., Randall, 2021), further refining the underlying algorithms and evaluating their performance across a range of conditions becomes crucial.

Herein, we address this need by introducing a new two-dimensional implementation of STIV, which we refer to as 2D-STIV, specifically intended for application at the reach scale of tens to hundreds of km, as opposed to a single, isolated cross section. STIV was initially developed by Fujita et al. (2007), refined in the ensuing years (Fujita et al., 2019; Watanabe et al., 2021), and is now one of the most mature and widely used image velocimetry algorithms. We provide a more detailed description of the STIV algorithm in Section 5 but to provide some introductory context, we begin by identifying two factors that motivated us to explore STIV. First, our previous research focused on PIV, which, as the name implies, is predicated upon the existence of discrete, readily trackable particles. This assumption is seldom satisfied in natural channels, however, and seeding the flow with artificial tracers, as in (Biggs et al., 2022) and many other studies, is likely to be highly complex, if not impractical, in large rivers or for operational streamgaging. Seeding can also introduce a number of additional complications during analysis (e.g., Alongi et al., 2023). We

were thus drawn to STIV as an alternative algorithm capable of capturing not only the motion of distinct particles but potentially less well-defined, diffuse image textures such as deforming boils of suspended sediment (Legleiter & Kinzel, 2020), waves, or other patterns of water surface reflectance. Second, and more importantly, we saw an opportunity to generalize the STIV framework to provide a more complete characterization of complex flow fields in natural channels. Most previous applications of STIV have focused on a single cross section, with the algorithm providing estimates of velocity magnitude along a constant flow direction assumed to be perpendicular to that transect (Fujita et al., 2007). In this study, we build upon recent work by Han et al. (2021) to develop a new, two-dimensional implementation of STIV that is capable of inferring not only the magnitude but also the orientation of velocity vectors. Moreover, we designed the 2D-STIV algorithm for application at the reach scale, making predictions at grid nodes spatially distributed throughout a user-defined region of interest rather than a single predefined cross section. The new 2D-STIV algorithm is not contingent upon user identification of search lines and is thus better-suited to mapping full, extensive velocity fields than standard STIV workflows.

To assess the potential utility of 2D-STIV, we applied the algorithm to three test data sets: a simulated image sequence based on hydrodynamic model output and UAS-based videos from two natural rivers. As an initial benchmarking exercise, we evaluated the accuracy and precision of the flow fields inferred via 2D-STIV and compared their performance to that of two established PIV algorithms, per-frame pair PIV and ensemble PIV. The results of this analysis provide insight into the strengths and weaknesses of each algorithm and a preliminary appraisal of the feasibility of obtaining a more complete characterization of natural flow fields via 2D-STIV. To summarize, our objectives in this paper are to (1) introduce a two-dimensional implementation of STIV amenable to reach-scale application; (2) describe two different versions of the new algorithm, one that exhaustively evaluates all possible flow directions within a specified range and one that uses an optimization-based algorithm to infer the local flow direction; and (3) apply the two 2D-STIV algorithms to three test data sets and compare their performance to that of two established PIV algorithms.

2 | METHODOLOGY AND METHODS

In this section, we first introduce the three test data sets used to evaluate the various image velocimetry algorithms we considered in this study: a simulated image sequence based on hydrodynamic model output and UAS-based videos from two natural rivers. We then describe the new two-dimensional STIV algorithm we developed. Section 2.3 briefly summarizes the PIV algorithms we used for comparison with the 2D-STIV algorithm and their parameterization. Finally, Section 2.4 defines the metrics we used to evaluate the performance of each algorithm for each test data set.

2.1 | Test data sets

Development and testing of image velocimetry algorithms proceeds most efficiently when the expected output is known *a priori* and can

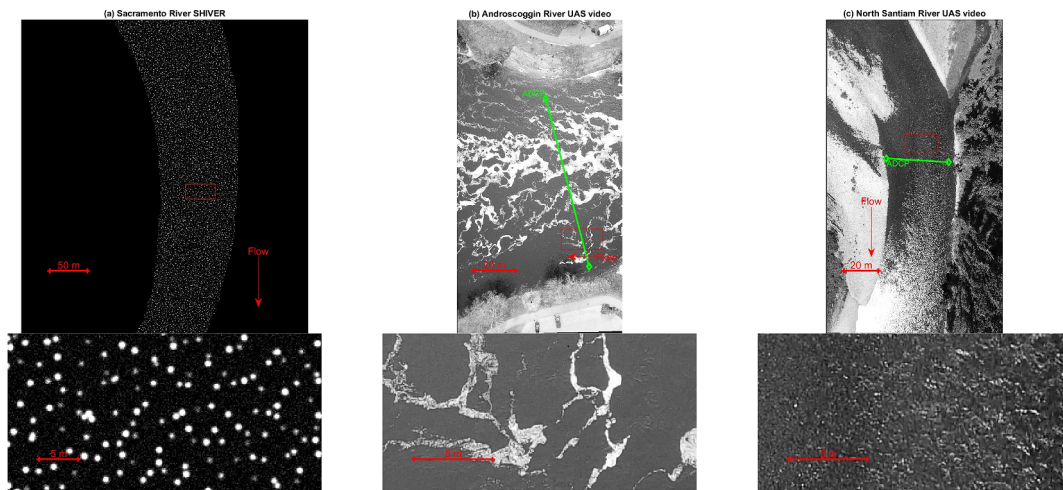


FIGURE 1 Example images from each study area: (a) simulated data based on the Sacramento River; (b) UAS-based video from the Androscoggin River; and (c) UAS-based video from the North Santiam River. For each site, the red box in the upper panel indicates the location of the zoomed subset in the lower panel. The locations of the cross sections along which an acoustic Doppler current profiler (ADCP) was used to make field measurements of flow velocity also are shown in (b) and (c). [Color figure can be viewed at [wileyonlinelibrary.com](https://onlinelibrary.wiley.com)]

be compared with the velocity estimates produced by the algorithm under consideration. Several previous studies have used simulated images for this purpose (Bodart et al., 2022; Dal Sasso et al., 2018; Mendes et al., 2020; Pumo et al., 2021), and we recently introduced a new workflow for Simulating Hydraulics and Images for Velocimetry Evaluation and Refinement (Legleiter & Kinzel, 2024). This approach, abbreviated SHIVER, involves combining a hydrodynamic model with a synthetic particle generator to produce a series of river images that capture the motion of simulated water surface features. The hydrodynamic model provides a plausible estimate of the flow field that is specific to the channel of interest and can be used to direct the advection of synthetic particles over time. Each of the resulting particle maps is rendered as an image to produce a sequence suitable for image velocimetry. The velocity estimates derived from this time series can then be compared with the known (modelled) flow field to evaluate the accuracy and sensitivity of the algorithm. For this study, we used SHIVER to generate a sequence of images for a 1.6 km reach of the Sacramento River in northern California, USA, with a mean width of approximately 110 m at a discharge of 255 m³/s. This time series consisted of 240 images at a frame rate of 4 Hz, with a pixel size of 0.15 m; the first frame in this sequence is shown in Figure 1a. The full 240-frame, 4 Hz sequence was used as input to 2D-STIV and per-frame pair PIV algorithms, but for the ensemble PIV algorithm, we used 60 frames at a lower frame rate of 1 Hz. Further details on the SHIVER framework and our study area along the Sacramento River are provided by Legleiter and Kinzel (2024); the data, hydrodynamic model archive, and source code used for this purpose are available from Legleiter and Kinzel (2023a).

As a complement to these synthetic images, we also considered videos acquired from UAS hovering in place above two natural rivers under typical low-flow conditions, without introducing any kind of artificial tracers. The first of these data sets was acquired along the Androscoggin River in Maine, USA to support the study of Duan et al. (2023) and is available from Engel et al. (2022). These two publications provide further detail on the site and data collection, but the key pieces of information most relevant in the present context are that the video was acquired at a frame rate of 24 Hz with a pixel size of

0.037 m and captures an 80 m reach of the river for which the mean width was approximately 94 m. A 10 s subset was extracted from the beginning of the original video to yield a 240 frame sequence for input to 2D-STIV and per-frame pair PIV algorithms. For the ensemble PIV algorithm, we used 90 frames extracted at a reduced frame rate of 1 Hz. Direct field measurements of flow velocity were also collected from the Androscoggin River by deploying an ADCP along a cross section located within the field of view of the UAS video (Figure 1b); the ADCP data were obtained on the same day as the video. We used the Velocity Mapping Toolbox (VMT Parsons et al., 2013) to produce a mean cross section from two passes across the channel and compute depth-averaged velocity vectors. Although we did not add any material to the Androscoggin to facilitate image velocimetry, our study site was located approximately 750 m below a waterfall that aerated the water and produced distinct patterns of foam and froth. These textural features are clearly evident in Figure 1b and presumably could be detected by the image velocimetry algorithms as they were advected downstream. The unique local geography of this site was thus highly conducive to remote sensing of surface flow velocities.

The second natural channel we examined provided a more realistic example in that neither artificial tracers nor fortuitous patterns of foam and froth were present. This data set was acquired from the North Santiam River in Oregon, USA, as part of an ongoing investigation of habitat suitability for salmonids. In this case, the clear water and lack of distinct surface tracer particles implied that any image-derived velocity estimates would have to be inferred from wave patterns and irregular reflections (i.e., sun glint) from the water surface itself (Figure 1c). We acquired UAS-based video of a 215 m reach of the North Santiam River with a mean width of approximately 40 m at a native frame rate of 30 Hz and a pixel size of 0.0472 m. For 2D-STIV and the per-frame pair PIV algorithm, we extracted 30 s of video at the full frame rate to obtain a 900-frame sequence. For ensemble PIV, we used a subsampled 1 Hz sequence spanning the entire duration of the video, yielding 31 frames. As for the Androscoggin, we used an ADCP to obtain direct measurements of flow velocity along a cross section within the footprint of the images and used VMT to

process these data and obtain depth-averaged velocities. Both the video and ADCP data are available from Legleiter and Harrison (2023).

We did not perform any kind of image preprocessing to increase the visibility of surface features in the UAS-based videos from the Androscoggin and North Santiam Rivers because our goal in this study was to assess the performance of the velocimetry algorithms using images *without* significantly enhancing them for this purpose. However, previous studies have shown that applying various filtering operations can improve velocity estimates (e.g., Ljubičić et al., 2024), suggesting that the results presented herein might be considered a lower bound on the performance of the algorithms we evaluated.

2.2 | A two-dimensional, reach-scale implementation of STIV

Like any image velocimetry algorithm, the fundamental input to our new, 2D implementation of STIV is a video or sequence of images. These data span a certain duration T and are captured at a specified interval dt , yielding a stack of $n_f = T/dt - 1$ image pairs at a frame rate of $1/dt$. To produce velocity estimates for a series of points along a cross section, as in most previous applications of STIV, or within a grid covering some larger region of interest encompassed by the image sequence, as in this study, the same core analysis is performed for each point in turn. For a given node, the other required inputs for STIV are the (x,y) image coordinates of the origin of a search line along which pixel values are extracted from the image time series, the length n_p of this search line in pixels, and an angle specifying the direction of the search line. This angle is essentially an initial guess for the primary flow direction at the current node and is denoted by ϕ_0 . For typical, cross section-based STIV, ϕ_0 is defined automatically as perpendicular to the cross section. In general, however, ϕ_0 will vary spatially throughout a reach. In our two-dimensional implementation, ϕ_0 thus becomes a function of (x,y) , but for brevity, we retain the same notation ϕ_0 . For 2D-STIV, we obtain a plausible initial estimate of the flow direction at any location along the channel by determining

the orientation of the centreline tangent vector at that streamwise position. This analysis is based on the Legleiter and Kyriakidis (2006) framework for converting from Cartesian (x,y) to channel-centred (s,n) coordinates and involves digitizing the line, representing this line as a series of cubic splines, and then using these polynomials to calculate the tangent vector for each vertex along the centreline.

Once the origin (x,y) , orientation ϕ_0 , and length n_p of a search line are specified in this manner, the next step in the workflow is to extract a space-time image (STI) along this line. To make this process more efficient, we first establish a gridded interpolant for the original, three-dimensional image sequence (i.e., a series of images stacked over time). This algorithm is much faster than standard functions for extracting pixel values along a profile and more flexible than direct indexing into an array. This initial phase of the 2D-STIV algorithm is illustrated in Figure 2a, which shows a simulated image of the Sacramento River generated via SHIVER with a search line beginning at $(x,y) = (1400,1250)$ and extending roughly downstream (southeast in this case, such that $\phi_0 = 160^\circ$) over a distance of $n_p = 50$ pixels. The resulting STI is shown in Figure 2b, with time (i.e., image frame number) as the horizontal axis and space (i.e., distance along the search line in units of pixels) as the vertical axis. This way of organizing the STI follows Han et al. (2021) but is transposed relative to the convention followed by Fujita et al. (2007) and many other applications of STIV. The representation adopted herein is more intuitive because ‘rise/run’ on the STI corresponds to units of velocity: space/time. In this case, the advection of simulated particles over time (i.e., from frame to frame) is depicted as white streaks steeply aligned from lower left to upper right.

In essence, STIV infers the velocity of the flow driving the motion of the water surface features captured in an STI by detecting streaks like those shown in Figure 2b and quantifying their orientation. To accentuate these streak lines and suppress background noise, the original STI is typically filtered prior to STIV analysis. Several filtering algorithms have been proposed (e.g., Fujita et al., 2020), but we found a relatively simple standardization filter described by Fujita et al. (2019) to be effective. The filter is applied independently to the rows of the STI, each of which represents a spatial position along the search

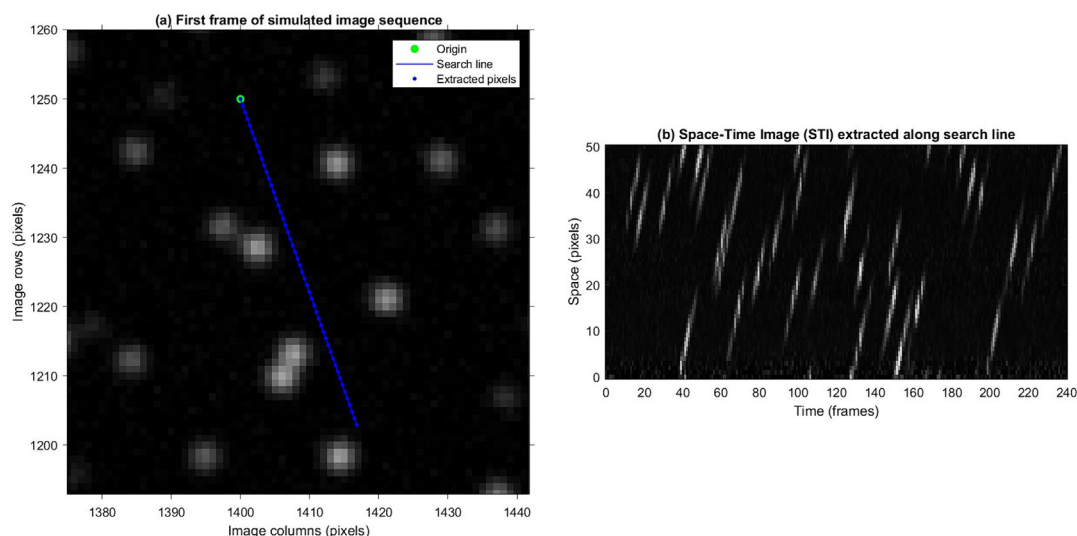


FIGURE 2 (a) Simulated image from the Sacramento River showing a search line oriented along the primary flow direction and the locations of pixels extracted along this line from each image in a sequence to construct the space-time image (STI) shown in (b). [Color figure can be viewed at [wileyonlinelibrary.com](https://onlinelibrary.com)]

line, and involves subtracting the time average (i.e., row mean) from each pixel and then dividing by the standard deviation of the pixel values along that row. This procedure is basically a statistical z-score transformation that serves to homogenize the distribution of image intensities in the original STI by normalizing the pixel values along each row to have a variance of 1.

One way to characterize the streaks evident in the resulting, filtered STI is to calculate its autocorrelation function (ACF, Fujita et al., 2019; Han et al., 2021), defined as

$$R(\tau_x, \tau_t) = \int_{-\infty}^{\infty} \int_{-\infty}^{\infty} f(x, t) f(x + \tau_x, t + \tau_t) dx dt \quad (1)$$

where $R(\tau_x, \tau_t)$ is the ACF value for a spatial lag of τ_x and a time lag of τ_t and $f(x, t)$ is the grayscale pixel value at location (x, t) in the filtered STI. In general, the cross-correlation of two arrays can be calculated as the convolution between the first array and the flipped version of the second array, so we obtained ACF values by convolving the filtered STI with the flipped version of itself. This algorithm is equivalent to the more complex alternative described by Fujita et al. (2019): calculating the ACF as the inverse Fourier transform of the power spectral density function of the filtered STI via the Wiener-Khinchin theorem (e.g., Krynkina et al., 2014). In any case, the ACF is then scaled to ensure a value of 1 at the origin; by definition, the correlation of any pixel in the STI with itself (i.e., when $\tau_x = 0$ and $\tau_t = 0$) is 1:

$$\hat{R}(\tau_x, \tau_t) = R(\tau_x, \tau_t) / R(0, 0) \quad (2)$$

Finally, the ACF is cropped to focus only on the central portion, beginning at the origin and extending in each direction by $\min(n_p/2, n_f/2)$. The original and cropped versions of the ACF calculated from the STI in Figure 2b are shown in Figure 3a and 3b, respectively. The purpose of the ACF is to summarize the texture present in the STI, with $\hat{R}(\tau_x, \tau_t)$ taking on relatively large values for combinations of the spatial and temporal lags τ_x and τ_t for which the pixel intensities at (x, t) and $(x + \tau_x, t + \tau_t)$ are similar. A high degree of similarity (i.e., correlation) occurs for pairs of pixels that are aligned along a streak, such that the highest values of $\hat{R}(\tau_x, \tau_t)$ are concentrated within an elongated ellipse inclined at an angle relative to the axes of the ACF. The correspondence between this tilted region of strong correlation and the streak lines in the STI makes the ACF a useful tool for detecting streaks and quantifying their primary orientation.

To make the relationship between the ACF and the angled streak lines in the STI more explicit, we follow Han et al. (2021) and convert the ACF from the Cartesian (τ_x, τ_t) coordinate system to a polar frame of reference, (θ, ρ) . This transformation is defined as

$$\theta = \tan^{-1}(\tau_t / \tau_x) \quad (3)$$

$$\rho = \sqrt{\tau_x^2 + \tau_t^2} \quad (4)$$

where the angle θ represents a direction in the (τ_x, τ_t) space of the original ACF and ρ denotes a radial distance from the origin along a ray in that direction. The polar ACF $\hat{R}(\theta, \rho)$ derived from the cropped Cartesian ACF $\hat{R}(\tau_x, \tau_t)$ in Figure 3b is shown in Figure 3c, with the axes of the former plot representing lines of constant θ and contours of ρ . Although the original ACF grid is regularly spaced in the (τ_x, τ_t) reference frame, the polar ACF in (θ, ρ) coordinates is irregular due to the nonlinearity of the transformation given by Equations (3) and (4), which dictates that the spacing between lines of constant θ increases as ρ increases. To obtain values of $\hat{R}(\theta, \rho)$ at constant, regular intervals of θ and ρ , we set up a gridded interpolant of $\hat{R}(\tau_x, \tau_t)$, create a series of rays emanating from the origin at an angular interval $d\theta$, and then query the interpolant at points spaced along each of these rays at a radial interval $d\rho$.

The angle θ_{max} along which the correlation is greatest is related to the orientation of the streak lines in the STI from which the ACF was derived. To identify this angle, the polar ACF is integrated over ρ along each ray of constant θ to obtain the area under the curve for a profile across the ACF surface in that direction:

$$F(\theta) = \int_0^{\rho_{max}} \hat{R}(\theta, \rho) d\rho \quad (5)$$

where

$$\rho_{max} = \min(\max(\theta_x), \max(\theta_t)) = \min(n_p/2, n_f/2) \quad (6)$$

$F(\theta)$ is maximized for the angle θ_{max} corresponding to the tilt of the predominant streak lines in the STI (Han et al., 2021). The value of θ_{max} is then used to calculate the velocity magnitude U as

$$U = \frac{S_x}{S_t} \tan(\theta_{max}) \quad (7)$$

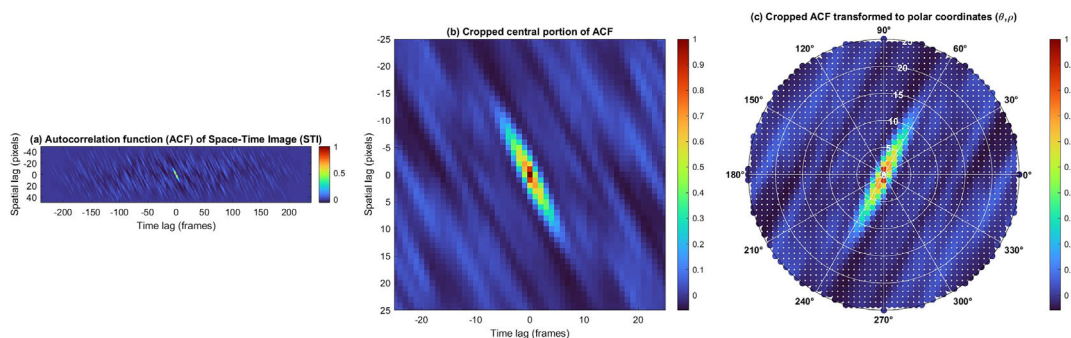


FIGURE 3 (a) Autocorrelation function (ACF) calculated from the space-time image (STI) shown in Figure 2b. (b) Cropped version of the ACF shown in (a) to focus on the area near the origin. (c) ACF transformed to polar coordinates. [Color figure can be viewed at wileyonlinelibrary.com]

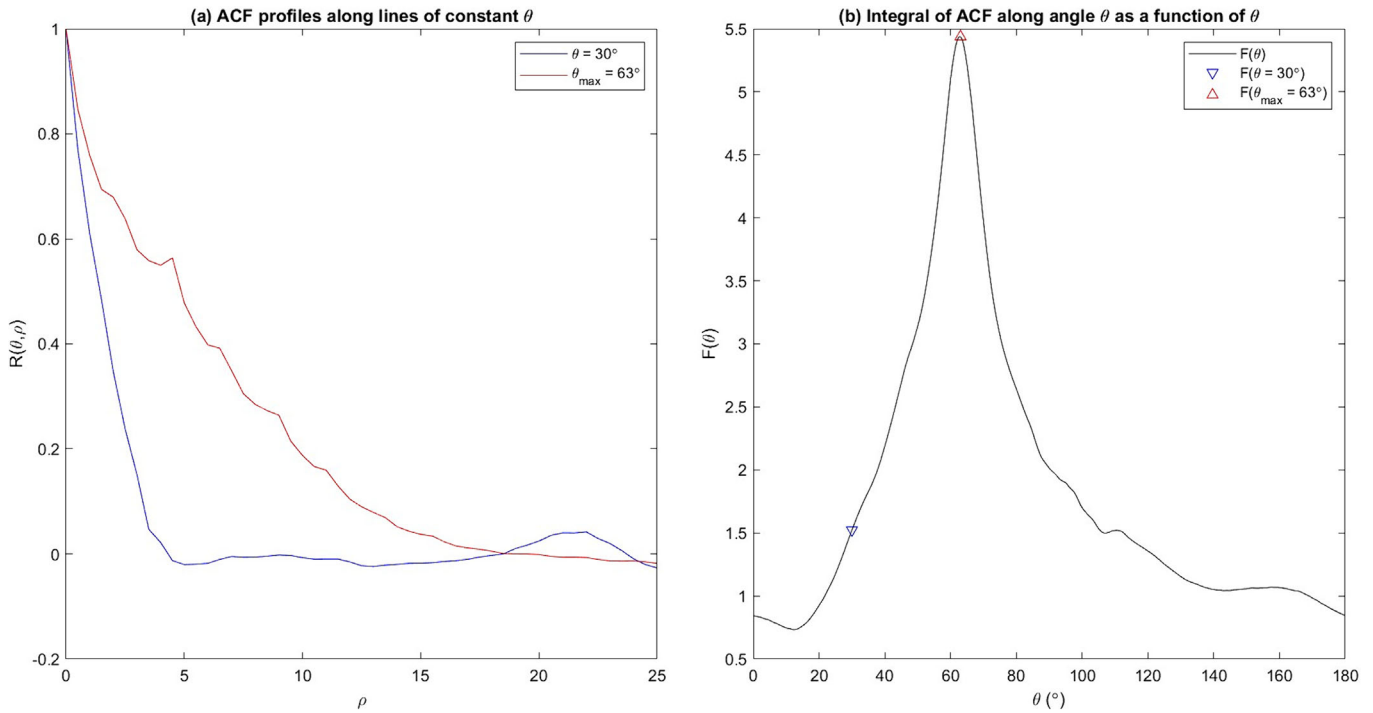


FIGURE 4 (a) Autocorrelation function (ACF) profiles along two lines of constant angle θ , the latter of which is the angle θ_{max} for which the radial integral $F(\theta)$ is maximized. (b) Radial integral values for all angles θ , with the two examples depicted in (a) indicated by point symbols. [Color figure can be viewed at wileyonlinelibrary.com]

where S_x is the size of an image pixel in meters and $S_t = dt$ is the image capture interval in seconds (Fujita et al., 2019). This process is illustrated in Figure 4. In the first panel, two example profiles across the polar ACF surface along lines of constant θ are plotted: an arbitrarily selected value of 30° and the angle θ_{max} that maximizes the area under the curve (i.e., $F(\theta)$). Figure 4b shows how the radial integral $F(\theta)$ varies as a function of θ over the full range from 0° to 180° , including the well-defined peak at θ_{max} . This angle corresponds to the orientation of the streak lines in the STI and can thus be used to calculate the velocity magnitude via Equation (7). For the pixel size ($S_x = 0.15$ m) and capture interval ($S_t = dt = 0.25$ s) used to simulate the image sequence upon which this example is based, this calculation leads to a plausible velocity estimate of 1.18 m/s.

The algorithm described so far is analogous if not equivalent to previous implementations of STIV (e.g., Fujita et al., 2019) and is one-dimensional, providing an estimate of the velocity magnitude along a search line with a single, predefined orientation. To extend STIV to two dimensions, we build upon previous work by Han et al. (2021) and repeat the preceding analysis for a range of search lines, each with a unique direction ϕ defined as an angle in the horizontal (x, y) plane. A separate STI is extracted along each of these lines and the ACF calculations described above are then repeated for each STI. To select the search line that corresponds to the primary flow direction, we define the function $p(\phi)$ as the maximum value of $F(\theta)$ over all angles θ for a given search line orientation ϕ :

$$p(\phi) = \max_{\theta=0}^{\theta=180} [F(\theta)] \quad (8)$$

The value of ϕ that yields the highest p , and thus the highest velocity magnitude via Equation (7), is the flow direction for the

current search line origin. We implement this strategy for a given node by radiating a collection of candidate search lines from the common origin located at (x_0, y_0) at directions ranging from $\phi_0 - \phi_r$ to $\phi_0 + \phi_r$ in steps of $d\phi$, where ϕ_0 is an initial estimate of the flow direction, ϕ_r specifies the range of directions to be considered, and $d\phi$ specifies the angular resolution. For example, to evaluate the entire forward (i.e., downstream) hemisphere for a channel with a primary flow direction of due south, ϕ_0 would be 180° in the geographic convention most often used by Earth scientists, which is equivalent to -90° or 270° in the mathematical convention, and ϕ_r would be set to 90° ; setting $d\phi = 1^\circ$ would provide a flow direction estimate to the nearest degree. This process is illustrated in Figure 5a, which shows a full set of 180 candidate search lines, each extending n_p pixels from their shared origin represented by the green circle at (x_0, y_0) but in a distinct direction ϕ . The peak value $p(\phi)$ of the radial integral along each of these search lines is plotted in Figure 5b. In this case, $p(\phi)$ is maximized for a search line oriented at a mathematical angle of 265° , which is 5° to the west relative to the initial guess ϕ_0 for the flow direction.

To perform a full, reach-scale two-dimensional STIV analysis, this process can be repeated at each node of a grid spanning some region of interest captured by the image sequence. For each node, the search line origin (x_0, y_0) is defined as the centre of the grid cell and the initial guess for the flow direction ϕ_0 is given by the centreline tangent vector at that location. At this stage, our algorithm diverges into two branches: an exhaustive version that explicitly evaluates each one of a specified set of candidate search lines and an optimization-based version that identifies the flow direction which maximizes $p(\phi)$. We refer to the exhaustive and optimization-based algorithms as 2D-STIV-E and 2D-STIV-O, respectively. Both of these functions take as input the original image sequence, the (x, y) coordinates of the grid nodes,

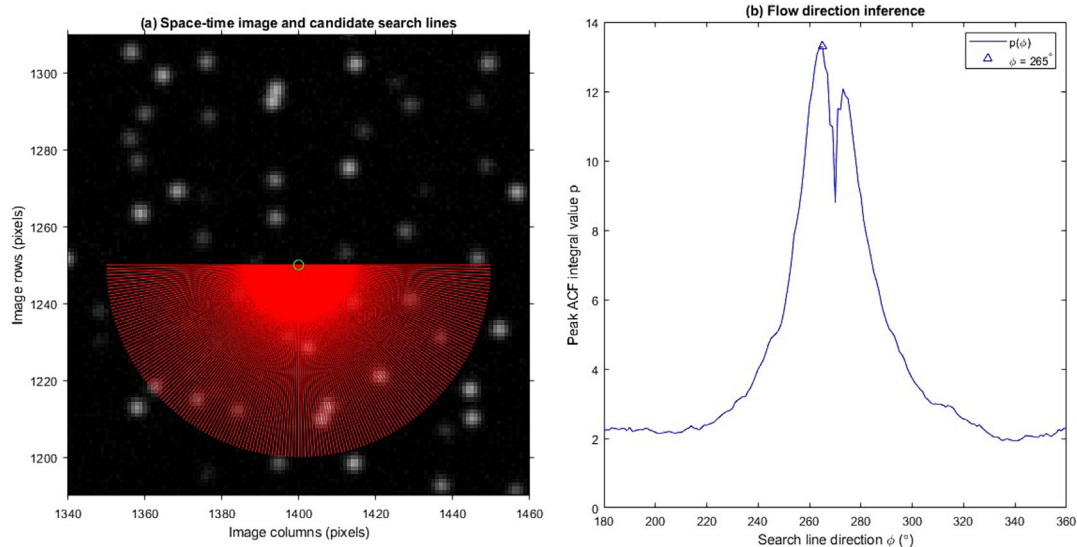


FIGURE 5 (a) Candidate search lines radiating from the common origin indicated by the green circle overlain on the original space-time image (STI), each oriented in a distinct direction ϕ . (b) Evaluating the radial integral of the autocorrelation function (ACF) along each of these lines and identifying the ϕ value for which the maximum of this integral is greatest provides an estimate of the flow direction. [Color figure can be viewed at wileyonlinelibrary.com]

an initial guess of the flow direction ϕ_0 at each one of these nodes, and the length n_p of the search line in pixels, along with the pixel size and capture interval needed to scale the velocity magnitude estimates via Equation (7). In addition, for 2D-STIV-E, the user must specify the angular resolution $d\phi$ and the range of directions ϕ_r to be considered, as described above. Given these inputs, 2D-STIV-E is implemented using a double for loop, with the outer loop over the nodes and the inner loop over the candidate search line orientations for the current node. The optimization algorithm is largely the same, but the inner loop over the potential flow directions is replaced by a call to a minimization algorithm (e.g., `fminsearch` in MATLAB MathWorks, 2024 or `minimize_scalar` in Python Python.org, 2024), which in turn evaluates an objective function that returns the negative of $p(\phi)$ for a given flow direction ϕ . Due to the negative sign, the lowest value of the objective function corresponds to the highest value of $p(\phi)$, and the corresponding ϕ is taken to be the flow direction for the current node. Both 2D-STIV-E and 2D-STIV-O yield the same type of output: an estimate of the velocity magnitude U and flow direction ϕ for each grid node. These results can be transformed to Cartesian vector components u and v as follows:

$$u = U \cos(\phi) \quad (9)$$

$$v = U \sin(\phi) \quad (10)$$

The resulting velocity field can then be plotted, typically as a magnitude (U) grid with (u, v) vectors overlain to indicate flow direction.

2.3 | Particle image velocimetry (PIV) algorithms, parameterization, and postprocessing

As an initial test of this new two-dimensional implementation of STIV, we compared the exhaustive and optimization-based versions to one another and to a pair of established PIV algorithms. The first,

per-frame pair PIV, is a cross-correlation-based algorithm developed by Thielicke and Sonntag (2021) as part of the PIVlab software package. Per-frame pair PIV is implemented in the frequency domain using a discrete Fourier transform and is applied to successive image pairs throughout a sequence to yield a distinct velocity field for each time increment. The resulting velocity estimates can then be time-averaged over the entire duration to provide a single, mean velocity field, or examined independently to quantify temporal variations in the flow and characterize turbulence (e.g., Duan et al., 2023).

The second PIV algorithm we considered is an ensemble correlation algorithm that is available within PIVlab and was recently adapted for application to nadir-viewing river images as part of the Toolbox for River Velocimetry using Images from Aircraft (TRIVIA Legleiter & Kinzel, 2023b). The ensemble PIV algorithm is well-suited to situations where the density of trackable features is low, but the flow can be assumed steady over time. These conditions are often satisfied in rivers, particularly if no artificial tracers are introduced and the duration of the image sequence is on the order of one minute. Because the ensemble PIV algorithm involves first calculating correlation matrices for successive image pairs and then averaging these matrices before applying a peak-finding algorithm, ensemble PIV can yield an improved signal-to-noise ratio and thus more robust velocity estimates than the original per-frame pair PIV algorithm (Thielicke & Sonntag, 2021).

For both the per-frame pair and ensemble PIV algorithms, three passes with successively smaller interrogation area (IA) sizes were performed. The final IA size was set to 50 pixels for all three sites, with the PIV step size set to half the IA. This parameterization led to a grid spacing (i.e., distance between output velocity vectors) of 3.75, 0.92, and 1.18 m for the Sacramento, Androscoggin, and North Santiam Rivers, respectively. For consistency, we used the same grid spacing for the 2D-STIV-E and 2D-STIV-O algorithms by setting the search line length n_p to 50 pixels for all three sites. Velocity estimation grids were generated by creating regularly spaced points with the specified spacing and then retaining only those nodes located within a region of

TABLE 1 Summary of image sequence characteristics and velocimetry algorithm parameterization for all 12 combinations of site and algorithm.

Site	Pixel size (m)	Algorithm	Frame rate (Hz)	Frames	Grid spacing (pixels)	Grid nodes	Parameters
Sacramento	0.15	2D-STIV exhaustive	4	240	25	3247	$n_p = 50, \phi_r = 90^\circ, d\phi = 1^\circ$
		2D-STIV optimization	4	240	25	3247	$n_p = 50$
		Per-frame pair PIV	4	240	25	3225	IA = 50
		Ensemble PIV	1	60	25	3237	IA = 50
Androscoggin	0.037	2D-STIV exhaustive	24	240	25	9096	$n_p = 50, \phi_r = 15^\circ, d\phi = 1^\circ$
		2D-STIV optimization	24	240	25	9096	$n_p = 50$
		Per-frame pair PIV	24	240	25	8890	IA = 50
		Ensemble PIV	1	90	25	9107	IA = 50
North Santiam	0.047	2D-STIV exhaustive	30	900	25	2990	$n_p = 50, \phi_r = 15^\circ, d\phi = 1^\circ$
		2D-STIV optimization	30	900	25	2990	$n_p = 50$
		Per-frame pair PIV	30	900	25	2987	IA = 50
		Ensemble PIV	1	31	25	2998	IA = 50

Abbreviations: ϕ_r , range of angles considered; $d\phi$, angular resolution; 2D-STIV, two-dimensional space-time image velocimetry; IA, interrogation area used in PIV; n_p is the search line length; PIV, particle image velocimetry.

interest digitized to encompass the wetted channel. For initial testing and development of the 2D-STIV-E algorithm using simulated data from the Sacramento River, we considered the full forward hemisphere (i.e., $\phi_r = 90^\circ$), but for the UAS-based videos from the Androscoggin and North Santiam Rivers, we limited the range of directions to $\phi_r = 15^\circ$ to reduce the computational burden. In all cases, the angular resolution for 2D-STIV-E was set to $d\phi = 1^\circ$. The image characteristics and parameterization for all 12 combinations of site and algorithm are summarized in Table 1.

To facilitate comparison across the four algorithms, we applied the same postprocessing procedures to the initial velocity fields produced by each algorithm. This phase of the analysis involved filtering the velocity estimates to exclude those with magnitudes below 0.1 m/s or above 5 m/s. Outliers were removed by discarding any velocity estimates that were more than four standard deviations from the global mean within the region of interest. More local filtering was accomplished by removing any velocity estimates that were more than 1.5 m/s above or below the median value within a 3×3 moving window. All values rejected by these filtering operations were replaced with NaNs (short for not a number and essentially serving as a no data value). In addition, we applied the infilling and smoothing tools available within PIVlab to the filtered velocity fields from all four image velocimetry algorithms to produce the final output.

2.4 | Accuracy assessment and metrics for comparison

We evaluated the performance of each velocimetry algorithm for each test data set and enabled comparisons across the various study sites and algorithms by calculating a series of metrics. For the simulated data from the Sacramento River generated via SHIVER, we compared image-derived velocity estimates to the known (modelled) flow field throughout the entire simulated image domain. For the UAS-based videos from the Androscoggin and North Santiam Rivers, velocities

inferred via the four image velocimetry algorithms were compared with depth-averaged velocities measured in the field with an ADCP. The image-derived velocity estimate at a given grid node was compared with the mean of all ADCP measurements located within a specified search radius of that node; the search radius was set to half the grid node spacing. The following metrics were then calculated for each combination of algorithm and site: observed (modelled for SHIVER-generated data or measured with an ADCP for the UAS-based videos) vs. predicted (via image velocimetry) (OP) regression R^2 , normalized mean bias, and normalized root mean squared error (RMSE). The latter two metrics quantified the accuracy and precision of image-derived velocity estimates, respectively, and were calculated as

$$\text{Normalized Mean Bias} = \frac{\sum_{i=1}^n (v_{p,i} - v_{m,i})}{n \cdot \bar{v}_m} \quad (11)$$

$$\text{Normalized RMSE} = \frac{\sqrt{\sum_{i=1}^n (v_{p,i} - v_{m,i})^2}}{n \cdot \bar{v}_m} \quad (12)$$

In these expressions, the subscript i denotes the i^{th} velocity vector and serves to index different locations, $v_{p,i}$ is the velocity inferred from the simulated image sequence or UAS-based video, $v_{m,i}$ is the known velocity from the model run used as input to SHIVER or measured in the field with an ADCP, n is the total number of velocity vectors being compared, and \bar{v}_m is the mean velocity from the flow model or ADCP. Dividing by \bar{v}_m essentially scales the bias and RMSE so that these metrics can be expressed as a proportion of the reach-averaged mean velocity.

In addition, we also calculated three more advanced metrics that provide information on the agreement between observed and predicted velocities not only in terms of magnitude but also vector orientation: the weighted relevance, weighted magnitude, and

combined magnitude and relevance indices. These metrics are described in greater detail by Willman et al. (2020) and Legleiter et al. (2023) and were calculated using a module from TRIVIA (Legleiter & Kinzel, 2023b). Briefly, the weighted relevance index (WRI) quantifies the degree of alignment between two sets of vectors, with greater weight given to higher velocities. If the observed and predicted vectors were perfectly aligned, the WRI would be 0, whereas a WRI of 0.5 would indicate a 90° misalignment. Similarly, the weighted magnitude index (WMI) quantifies the agreement between two velocity fields solely in terms of magnitude by dividing the difference in vector magnitude at a given location by the median of all the magnitudes in either version of the velocity field. Two vectors with the same magnitude yield a WMI of 0 and vectors that differ greatly in magnitude lead to $WMI > 1$. Finally, because a strong agreement between velocity fields in terms of orientation does not guarantee a good agreement in terms of magnitude and vice versa, the combined magnitude and relevance index (CMRI) summarizes the two criteria as the average of the WRI and WMI. Calculating these three metrics leads to distributions of index values that can be summarized via histograms and maps that highlight spatial variations in the level of agreement between observed and predicted velocities (Legleiter et al., 2023; Legleiter & Kinzel, 2023b). In addition, we recorded the total computational run time for each combination of site and algorithm and calculated the run time per velocity estimation node to facilitate comparison.

3 | RESULTS

In this section, we first present results from each site, including the velocity fields produced by the four image velocimetry algorithms (exhaustive and optimization-based 2D-STIV and per-frame pair and ensemble PIV) and assessments of their accuracy. For each site, the image-derived velocity fields are displayed as grids coloured by magnitude with vectors overlain to indicate flow direction, both at the reach scale and as zoomed-in subsets at the locations indicated by the red boxes in Figure 1. The accuracy assessment figure for each site consists of a plot of the observed (modelled or measured) versus predicted (image-derived) velocities with the OP regression line shown in blue and the one-to-one line of perfect agreement dashed in black. The middle and right columns of these figures present histograms and maps of the WRI, the metric we used to quantify the level of agreement between the flow directions inferred from the images and those modelled via SHIVER or measured in the field with an ADCP. The WRI ranges from 0 to 0.5, with 0 indicating perfectly aligned vectors and a value of 0.5 implying that the vectors are perpendicular to one another. Finally, in Section 5, we synthesize results across the three sites and four image velocimetry algorithms we evaluated in both tabular and graphical form.

3.1 | Image velocimetry based on simulated data from the Sacramento River

As a starting point for developing a new reach-scale, two-dimensional implementation of STIV, we used the SHIVER framework to generate a plausible sequence of images for a reach of the Sacramento River. Because the flow field leading to this simulated image sequence was

based on a hydrodynamic model, the velocity estimates derived from both the new 2D-STIV algorithms and existing PIV algorithms could be compared directly to the known velocities throughout the reach. This approach allowed us to verify the performance of the velocimetry algorithms by evaluating their ability to reproduce the modelled flow field. The velocity magnitude grids shown in Figure 6 are all very similar to one another, essentially indistinguishable when plotted at the reach scale or when zoomed in. All four algorithms capture the general structure of the flow through this gentle meander bend, with higher velocities at the upper end of the study area and along the outer bank and slower flow over the point bar and toward the lower end of the reach.

Accuracy assessment of these flow fields via comparison to the known (modelled) velocities also led to consistent results across the four algorithms, as summarized in Figure 7. Agreement between observed and predicted velocities was very strong for all four algorithms, with $R^2 > 0.97$ for both 2D-STIV implementations and for the ensemble PIV algorithm. The correspondence between modelled and image-derived velocities was slightly weaker for the per-frame pair PIV algorithm, with an R^2 of 0.931. All four algorithms yielded velocity estimates that were essentially unbiased, with normalized mean bias values on the order of -0.01 m/s, with the negative sign indicating a slight tendency to underpredict velocity magnitudes relative to the flow model. The estimates were also highly precise, with normalized RMSE values ranging from 0.03 m/s for both 2D-STIV algorithms and ensemble PIV to 0.05 m/s for per-frame pair PIV. Moreover, the WRI histograms in Figure 7 indicate that the vast majority of the image-derived vectors are closely aligned with those from the hydrodynamic model. The WRI maps show that nearly all vectors throughout the study area had WRI values near 0. The only exception, which is obscured when plotted at this scale, is at the entrance to the reach, where edge effects might lead to some discrepancies in flow direction. Overall, these results indicate that the new 2D-STIV algorithms were capable of taking a series of simplified, simulated images as input and reproducing the known flow field upon which the simulations were based. In addition, the accuracy of both the exhaustive and optimization-based 2D-STIV implementations was comparable to that of two established PIV algorithms.

3.2 | Image velocimetry based on aerial video from the Androscoggin River

As an initial test of the new 2D-STIV algorithms using real-world data, we applied both the exhaustive and optimization-based versions to video acquired from the Androscoggin River via UAS. Our study area was located immediately below a waterfall that introduced distinct streaks of foam and froth to the river downstream (Figure 1b). We hypothesized that these conditions would facilitate image velocimetry by serving as natural tracers, expressed as variations in image brightness, that could be detected and tracked by the various algorithms. The velocity fields generated via the exhaustive and optimization-based 2D-STIV algorithms and the per-frame pair and ensemble versions of PIV are shown in Figure 8, which highlights some important differences among the four algorithms.

The new 2D-STIV algorithm led to reasonable velocity estimates for much of the reach but also featured patches with irregular vectors,

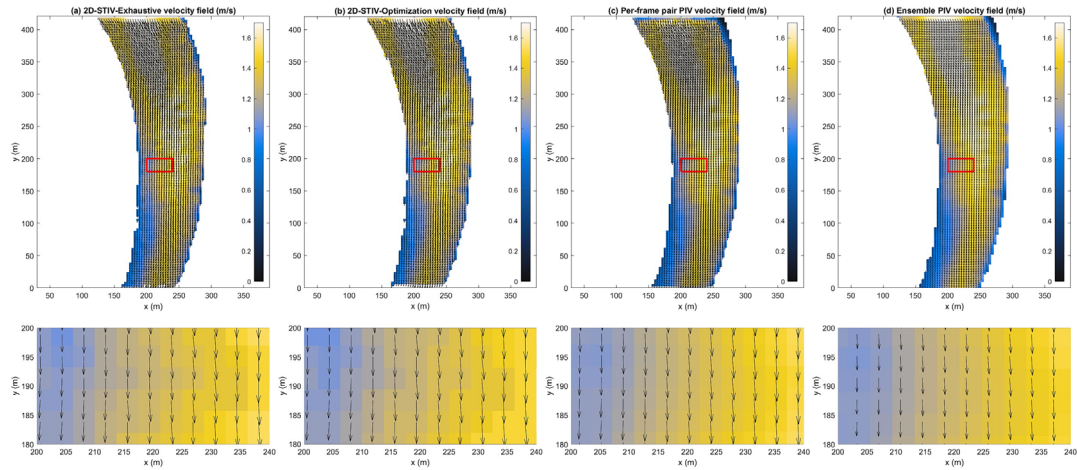


FIGURE 6 Velocity fields inferred from simulated image data from the Sacramento River using four different image velocimetry algorithms: (a) the exhaustive implementation of two-dimensional space-time image velocimetry (2D-STIV); (b) the optimization-based implementation of 2D-STIV; (c) per-frame pair particle image velocimetry (PIV); and (d) ensemble PIV. The red boxes in the upper panels indicate the location of the zoomed subsets in the lower panel and are the same for all four algorithms. [Color figure can be viewed at wileyonlinelibrary.com]

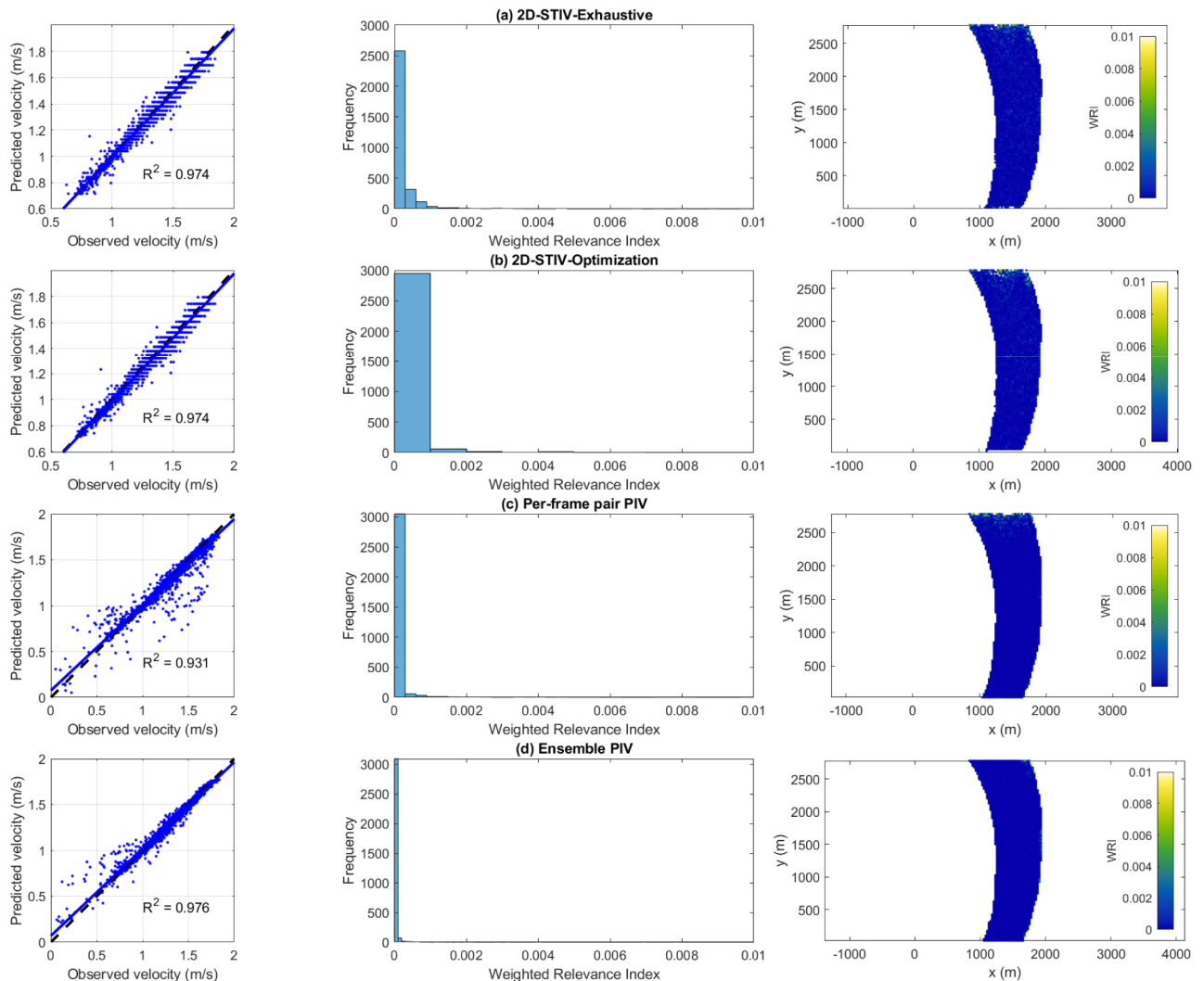


FIGURE 7 Observed (modelled) versus predicted (image-derived) regression results and histograms and maps of the weighted relevance index for simulated image data from the Sacramento River using four different image velocimetry algorithms: (a) the exhaustive implementation of two-dimensional space-time image velocimetry (2D-STIV-E); (b) the optimization-based implementation of 2D-STIV-O; (c) per-frame pair particle image velocimetry (PIV); and (d) ensemble PIV. [Color figure can be viewed at wileyonlinelibrary.com]

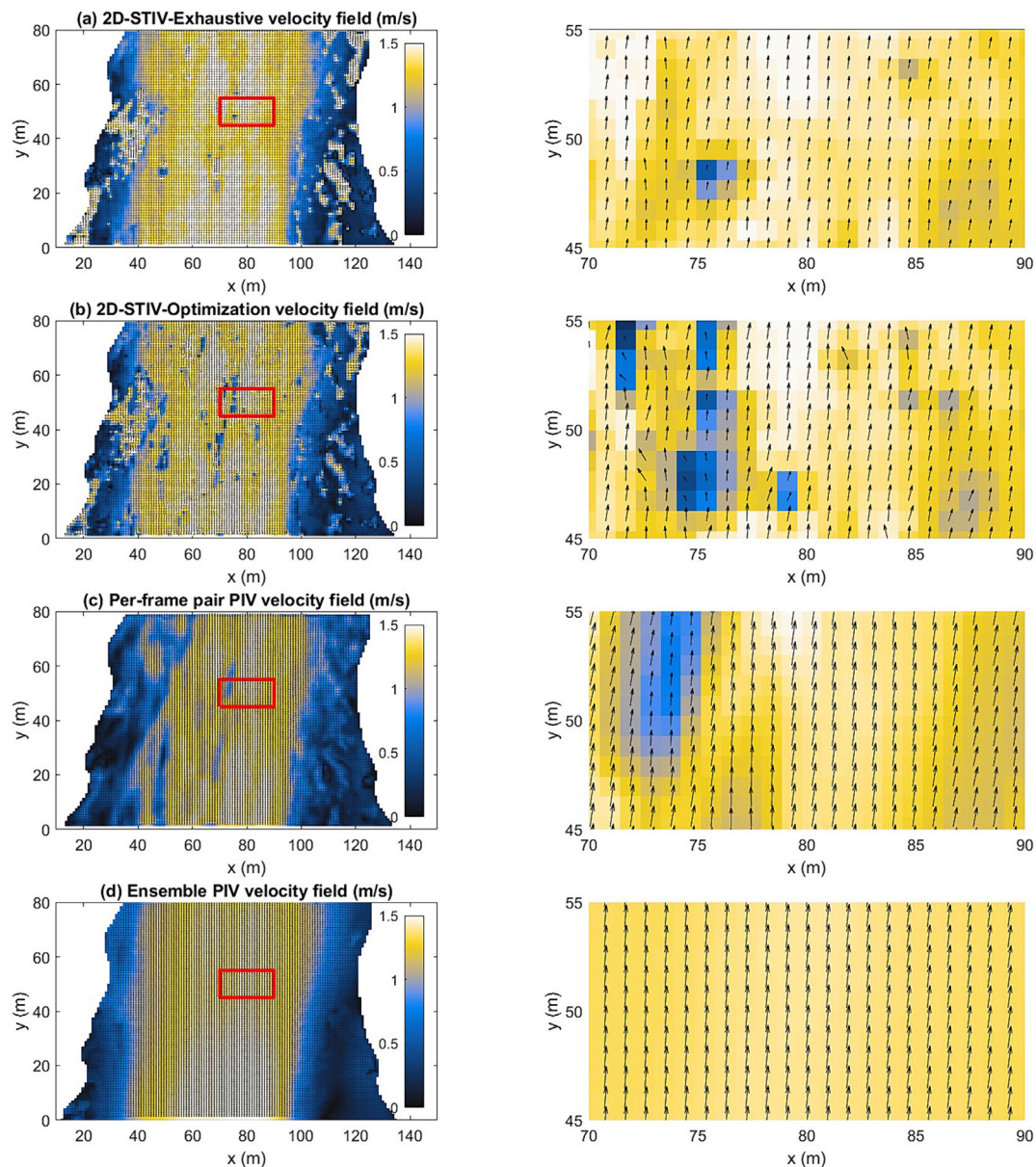


FIGURE 8 Velocity fields inferred from aerial video from the Androscooggin River using four different image velocimetry algorithms: (a) the exhaustive implementation of two-dimensional space-time image velocimetry (2D-STIV); (b) the optimization-based implementation of 2D-STIV; (c) per-frame pair particle image velocimetry (PIV); and (d) ensemble PIV. The red boxes in the panels in the left column indicate the location of the zoomed subsets in the right column and are the same for all four algorithms. [Color figure can be viewed at wileyonlinelibrary.com]

such as those highlighted in the zoom subsets on the right side of Figure 8a and b. These noisy areas might have occurred where the foam patterns were not well-defined or were highly variable over time. Another plausible explanation could be that the local flow direction was not within the $\phi_r = \pm 15^\circ$ tolerance of the centreline tangent vector we used as an initial estimate of ϕ_0 for the exhaustive 2D-STIV implementation, which might have prevented the algorithm from producing reliable velocity estimates in these areas. Optimization-based 2D-STIV led to even noisier patterns in these locations because the parameter space searched by the algorithm encompassed the full range of flow directions. In fact, inspection of the zoom subsets in Figure 8a and b indicates that 2D-STIV-O yielded a markedly more erratic velocity field, with greater variation in both the magnitude and orientation of vectors. Imposing a constraint on the range of flow directions considered by 2D-STIV-E prevented this version of the algorithm from producing such irregular vector orientations but could

also preclude the algorithm from capturing more complex flow patterns with local deviations from the general downstream direction.

In contrast, the image-derived velocity fields produced by the PIV algorithms, shown in Figure 8c and d, had less localized noise. However, the per-frame pair PIV algorithm produced a velocity field that was much more variable than that generated via ensemble PIV, even when the initial per-frame pair output was time-averaged over 240 frames (10 s). At the scale of the entire image, the velocity field generated via per-frame pair PIV is patchy and irregular, with areas of very low velocity along the channel margins juxtaposed against isolated pockets of faster flow. Although a clear thalweg is evident, even in the centre of the channel the main flow is interrupted by elongated streaks of low velocity. These flow patterns could be an accurate reflection of nonstationary, turbulent conditions, but the macroscopic impression given by Figure 8c is a lack of organization. The output from the ensemble PIV algorithm, however, is smoother and more

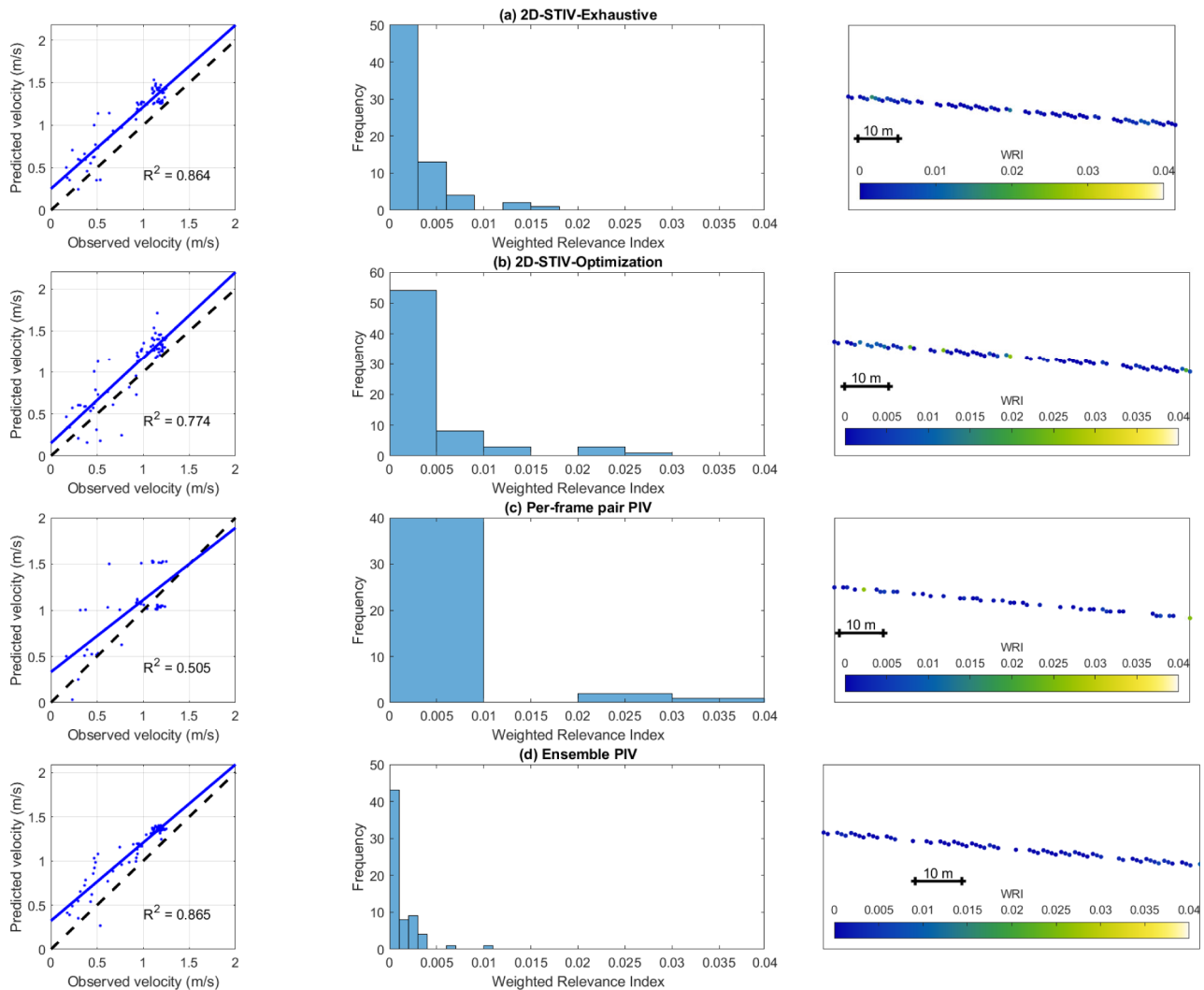


FIGURE 9 Observed versus predicted (image-derived) regression results and histograms and maps of the weighted relevance index for aerial video from the Androscoggin River using four different image velocimetry algorithms: (a) the exhaustive implementation of two-dimensional space-time image velocimetry (2D-STIV-E); (b) the optimization-based implementation of 2D-STIV-O; (c) per-frame pair particle image velocimetry (PIV); and (d) ensemble PIV. [Color figure can be viewed at [wileyonlinelibrary.com](https://onlinelibrary.wiley.com)]

coherent, with a well-defined thalweg and a more gradual transition to lower velocities along the banks. Performing PIV in three passes allowed larger-scale streamwise advection to be captured effectively by the initial passes with relatively coarse IAs before stepping down to progressively smaller IA sizes. The difference between the two PIV algorithms is quite pronounced in the zoom subsets, where the per-frame pair PIV-derived velocity field features an abrupt, localized low velocity zone that is absent from the ensemble PIV results. The averaging of correlation matrices by the latter algorithm led to a smoother representation of the time-averaged velocity field. Previous research also showed that image sequence duration had minimal impact on the accuracy of velocity estimates inferred via ensemble PIV (Legleiter & Kinzel, 2024). This coherence comes at the expense of temporal detail, however, and the ensemble algorithm cannot resolve higher-frequency fluctuations that might be captured by the per-frame pair algorithm and could be of primary interest for certain applications concerned with turbulence (e.g., Duan et al., 2023).

To quantitatively assess the accuracy of the four algorithms, we compared image-derived velocity estimates to direct field measurements of depth-averaged flow velocity made with an ADCP along the transect shown in Figure 1b, in which the example video frame was

transposed for display. The results of this analysis are summarized in Figure 9, which represents the full width of the cross section measured with an ADCP in the field. Because we were not attempting to calculate discharge, we did not extrapolate the ADCP data or the image-derived velocity estimates to the edges of the wetted channel. For the 2D-STIV algorithms, the OP regressions were similar but with stronger agreement between image-derived and field-measured velocities for the exhaustive implementation than for the optimization-based version. Both algorithms tended to overpredict the ADCP data, with normalized mean bias values of 0.247 and 0.195 for 2D-STIV-E and 2D-STIV-O, respectively. Because we did not attempt to convert image-derived velocities to depth-averaged velocities by using a measured or assumed α coefficient (Biggs et al., 2023), these overpredictions were expected. The presence of both low and high outliers for the latter algorithm led to a slightly higher normalized RMSE of 0.290. A more significant distinction between the exhaustive and optimization-based 2D-STIV algorithms was their level of agreement with field observations in terms of flow direction. The WRI histograms in Figure 9a and b have different scales, which indicate that although both algorithms yielded vectors that were well-aligned with the field data, 2D-STIV-O led to a longer tail of large WRI values

representing greater misalignment. The WRI maps suggest that the spatial pattern of flow direction error was similar for the two algorithms, with the largest discrepancies occurring at one point in the centre of the channel and on the left side of the maps, which corresponds to the right bank when facing downstream.

Performance differed substantially between the two PIV algorithms, with the ensemble algorithm yielding velocity estimates that were much more accurate than those produced on a per-frame pair basis. The regression plot in Figure 9c features two pronounced horizontal bands that represent points along the ADCP transect where the velocities measured in the field varied considerably while those inferred from the video remained relatively constant at about 1 and 1.5 m/s. This discrepancy reduced the overall correspondence and led to a modest OP R^2 of 0.505. The ensemble PIV algorithm, in contrast, yielded a much stronger relationship between image-derived velocity magnitudes and ADCP measurements, with an OP R^2 of 0.864. Velocities tended to be overestimated, with a normalized bias of 0.239, but this could be a consequence of comparing surface velocities derived

from the video to depth-averaged velocities calculated from the ADCP data without applying any kind of velocity index as a correction (Biggs et al., 2023). The per-frame pair PIV algorithm also led to less reliable estimates of flow direction, as indicated by the longer tail of high WRI values in Figure 9c than in 9d and a median WRI value over twice as large: 0.0011 for the per-frame pair algorithm versus 0.0005 for the ensemble algorithm. The spatial pattern of flow direction errors were similar for the two PIV algorithms but differed from the 2D-STIV algorithms, with the greatest discrepancies occurring on the right side of the maps for PIV, rather than on the left as for 2D-STIV.

3.3 | Image velocimetry based on aerial video from the North Santiam River

The data set from the second natural river we examined, the North Santiam, presented a more stringent test of the image velocimetry algorithms. Whereas the simulated data from the Sacramento

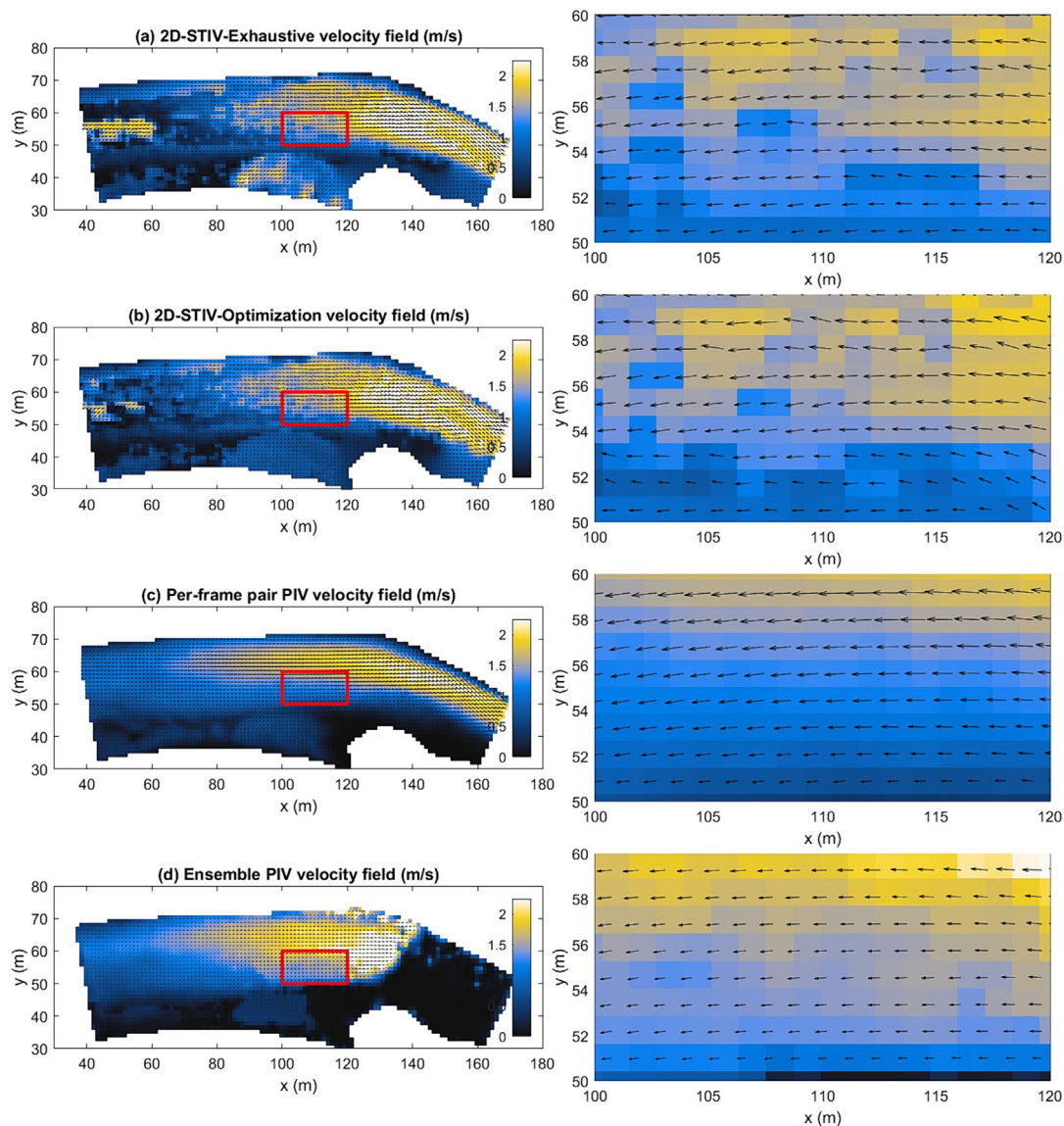


FIGURE 10 Velocity fields inferred from aerial video from the North Santiam River using four different image velocimetry algorithms: (a) the exhaustive implementation of two-dimensional space-time image velocimetry (2D-STIV); (b) the optimization-based implementation of 2D-STIV; (c) per-frame pair particle image velocimetry (PIV); and (d) ensemble PIV. The red boxes in the panels in the left column indicate the location of the zoomed subsets in the right column and are the same for all four algorithms. [Color figure can be viewed at [wileyonlinelibrary.com](https://onlinelibrary.wiley.com)]

consisted of idealized, spherical particles and the Androscoggin video featured distinct streaks of foam and froth, the North Santiam did not contain any obvious tracers, only rippled patterns of reflectance from the water surface. Although the advection of these textures was evident to the human eye when playing the video, the ability of the algorithms to detect such subtle motion remained uncertain. Velocity fields inferred from the North Santiam video using the new 2D-STIV and existing PIV algorithms are depicted in Figure 10. Relative to the example frame shown in Figure 1c, which was transposed for display, these velocity fields are rotated, with flow toward the left in Figure 10 corresponding with flow toward the bottom of Figure 1c. The velocity grids were also truncated to exclude the area of very bright sun glint that saturated the lower portion of the original images.

Qualitatively, the two versions of the new 2D-STIV algorithm yielded similar velocity fields, both when viewed at the reach scale and when zoomed in on a smaller subset (Figure 10a,b). The output from both algorithms became more patchy at the lower (left) end of the domain, where intense sun glint might have led to space-time images that lacked coherent streak lines, at least for the 50-pixel search lines we evaluated. The 2D-STIV algorithms captured the higher velocities at the upper (right) end of the reach but were erratic through the middle of the study area. The greater variation in flow direction resulting from the optimization-based algorithm was evident in Figure 10b, whereas constraining the range of search line orientations considered by the exhaustive implementation led to more uniform vectors (Figure 10a).

The two PIV algorithms yielded much smoother, more coherent velocity fields, particularly for the per-frame pair algorithm (Figure 10c). Neither of the PIV algorithms led to patchy output at the lower end of the reach where sun glint caused problems for 2D-STIV. In contrast to the Androscoggin, the per-frame pair version of PIV led to a more coherent velocity field than the ensemble algorithm, with the latter yielding a more irregular pattern of velocities with an abrupt transition from very low velocities spanning the full channel width at the upper end of the reach to much higher velocities in the middle of the study site. The thalweg in this area is also broader for the ensemble PIV-derived velocity field, as illustrated by the higher velocities at the top of the zoom subset for the ensemble PIV algorithm (Figure 10d) than for the per-frame pair algorithm (Figure 10c). These differences between PIV algorithms could be a consequence of temporally nonstationary image texture that affected velocity estimates less when they were computed as the time average of instantaneous velocity fields, as in the per-frame pair algorithm, than when the correlation matrices were averaged prior to peak finding, as in the ensemble algorithm.

Quantitative analysis of the four image-derived velocity fields based on comparisons to ADCP data collected along the transect shown in Figure 1c indicated that image velocimetry could still yield reasonably accurate velocity estimates even in the absence of discrete particles or obvious patterns like those present in the other two test data sets we examined. Accuracy assessment of the output from 2D-STIV-E revealed very poor agreement between image-derived and field-measured velocities, with the latter scattered about 1.5 m/s across a range of measured velocities from nearly 0 up to 2 m/s (Figure 11a). The reason for this poor performance is not immediately apparent but could be a consequence of the restricted range of search line orientations to which we constrained the exhaustive algorithm. The optimization-based 2D-STIV algorithm, in contrast, yielded a

much stronger relationship between image-derived and field-measured velocities, with an OP R^2 of 0.755, but with a tendency to overpredict velocities that was more pronounced in the slower areas of the flow. The two PIV algorithms led to similar levels of agreement with ADCP measurements, with OP R^2 values of 0.730 and 0.781 for the per-frame pair and ensemble implementations, respectively. Both algorithms tended to overpredict velocities, with normalized mean bias values of 0.325 and 0.491 that might result from comparing surface velocities to depth-averaged velocities. In terms of vector alignment, the two PIV algorithms had similar WRI values that were much smaller than those from the optimization-based 2D-STIV algorithm. For all four algorithms, the largest WRI values were concentrated in a zone toward the upper left of the maps in Figure 11, which corresponds to the right bank when facing downstream. The ADCP data and video footage both indicate that flow in this area is very slow or even recirculating back upstream, so the inability of the image velocimetry algorithms to capture these complex flow patterns was not unexpected.

3.4 | Synthesis and comparison of results across sites and algorithms

The accuracy assessments described on a site-by-site basis in the preceding subsections are represented graphically in Figure 12 as a series of bar charts grouped by site, with the four image velocimetry algorithms distinguished by bar colour. These results are also aggregated and summarized in Table 2. The metrics reported include measures of the agreement between the velocity magnitudes estimated from simulated or UAS-based image sequences and those predicted by the hydrodynamic model or measured in the field: OP regression R^2 , normalized bias, and normalized RMSE. A set of more advanced metrics (WRI, WMI, and CMRI) provided information on the correspondence between image-derived flow directions and the orientations of the modelled or measured velocity vectors; we summarized distributions of these metrics using the median. Finally, we provide a relative measure of the computational burden associated with each algorithm by reporting the run time per grid node.

The reliability of image-derived velocity estimates was greatest for the simulated data set from the Sacramento River, which consisted of highly idealized, spherical particles advected by a simple, modelled flow field. For this site, all four algorithms led to high OP R^2 values, ranging from 0.931 for per-frame pair PIV to 0.976 for ensemble PIV, and small, negative normalized biases of less than 1% of the mean flow velocity for the reach. Velocity estimates were also highly precise, with normalized RMSE values ranging from 3% to 5%. Metrics based on both magnitude and direction also indicated that the image-derived and modelled velocity vectors were consistently well aligned. Differences among the four algorithms were negligible for this site, providing confirmation that the new 2D-STIV algorithms were capable of reproducing a simple, known flow field with a level of fidelity similar to that of more established PIV algorithms.

The performance of all four algorithms was not as strong for the two natural rivers, with the metrics for the Androscoggin generally superior to those from the North Santiam. For both sites, the ensemble PIV algorithm led to the highest OP regression R^2 , with the per-frame pair algorithm leading to a value nearly as high for the North

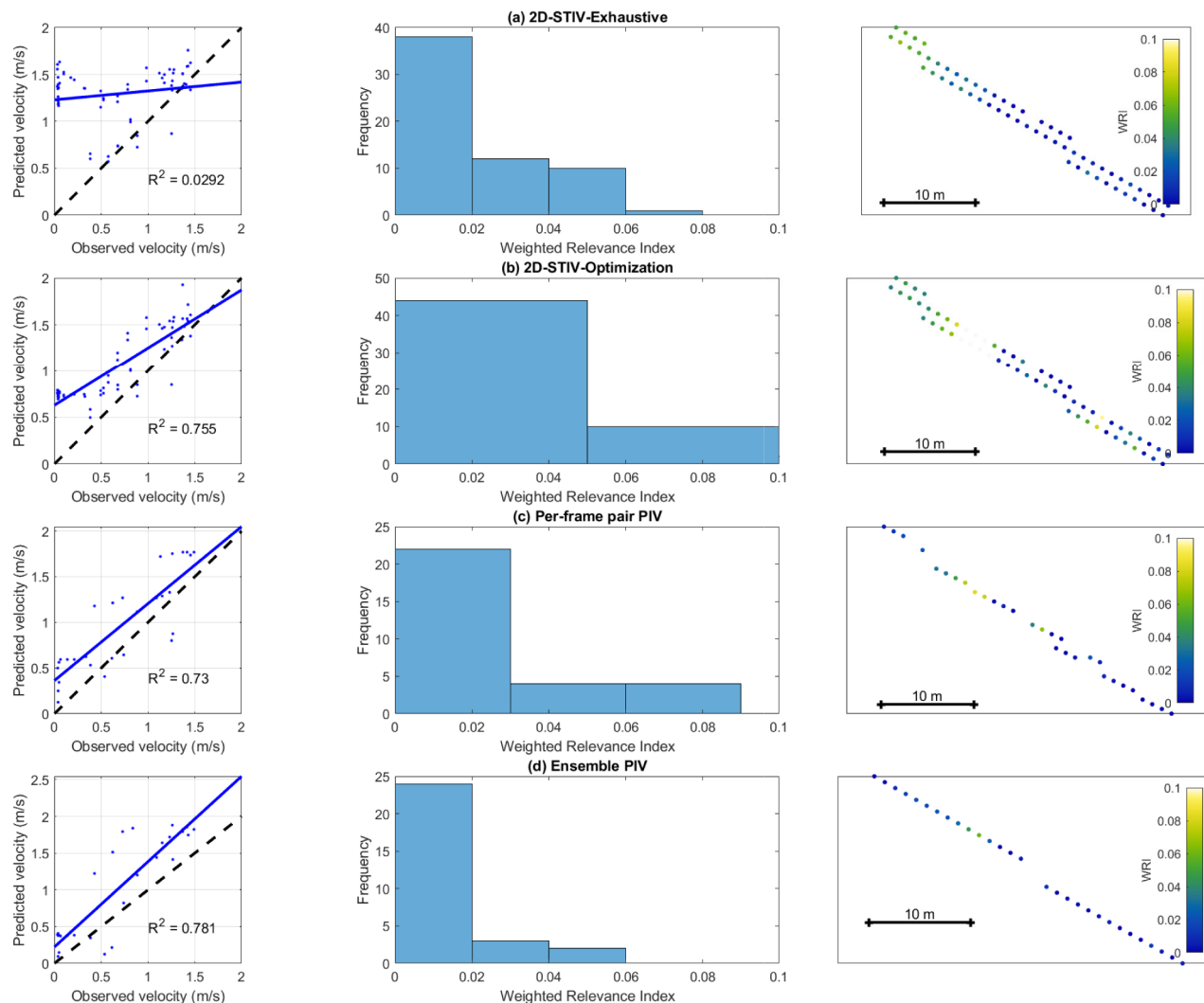


FIGURE 11 Observed versus predicted (image-derived) regression results and histograms and maps of the weighted relevance index for aerial video from the North Santiam River using four different image velocimetry algorithms: (a) the exhaustive implementation of two-dimensional space-time image velocimetry (2D-STIV-E); (b) the optimization-based implementation of 2D-STIV-O; (c) per-frame pair particle image velocimetry (PIV); and (d) ensemble PIV. [Color figure can be viewed at wileyonlinelibrary.com]

Santiam but substantially lower for the Androscoggin. Results from the 2D-STIV algorithms were more variable, ranging from highly reliable when the exhaustive implementation was applied to the Androscoggin to essentially uninformative when the same algorithm was used on the North Santiam. The metrics based on vector orientation also varied as a function of both site and algorithm, with higher values of the median WRI for the optimization-based version of 2D-STIV indicating a greater tendency to produce vectors that were not well-aligned with the ADCP observations. Because the exhaustive 2D-STIV algorithm was constrained to a $\pm 15^\circ$ tolerance about the initial estimate of flow direction, the image-derived velocity vectors were, by construction, less variable. Imposing such constraints would also preclude 2D-STIV-E from detecting more complex two-dimensional flow patterns, however.

Finally, the computational cost of the various image velocimetry algorithms followed a consistent trend across the three test data sets. As the name implies, the exhaustive implementation of the 2D-STIV algorithm required the longest run times on a per-node basis, whereas the optimization-based 2D-STIV algorithm was relatively efficient even though all possible flow directions were considered. The selection of a 2D-STIV algorithm might thus entail a trade-off between

reliability and speed. The most computationally efficient PIV algorithm was the ensemble algorithm, which involved averaging correlation matrices prior to peak finding. Although run times were longer when the PIV was performed on a per-frame pair basis, the per-frame pair PIV algorithm was capable of providing temporally detailed information on turbulence and unsteady flow conditions that would be obscured by ensemble PIV. The greatest run times for this study were for the exhaustive 2D-STIV and per-frame pair PIV algorithms for the North Santiam, where 900 frames at 30 Hz were provided as input to maximize the amount of data available to support inference of flow velocities from subtle patterns of water surface reflectance.

4 | DISCUSSION

In Section 2.2, we introduced a new, two-dimensional implementation of STIV that generalizes the original one-dimensional algorithm for reach-scale mapping of complex velocity fields in natural channels. Section 3 then presented results from the application of two different versions of the new 2D-STIV algorithm to three different test data sets and compared their performance to that of two established PIV

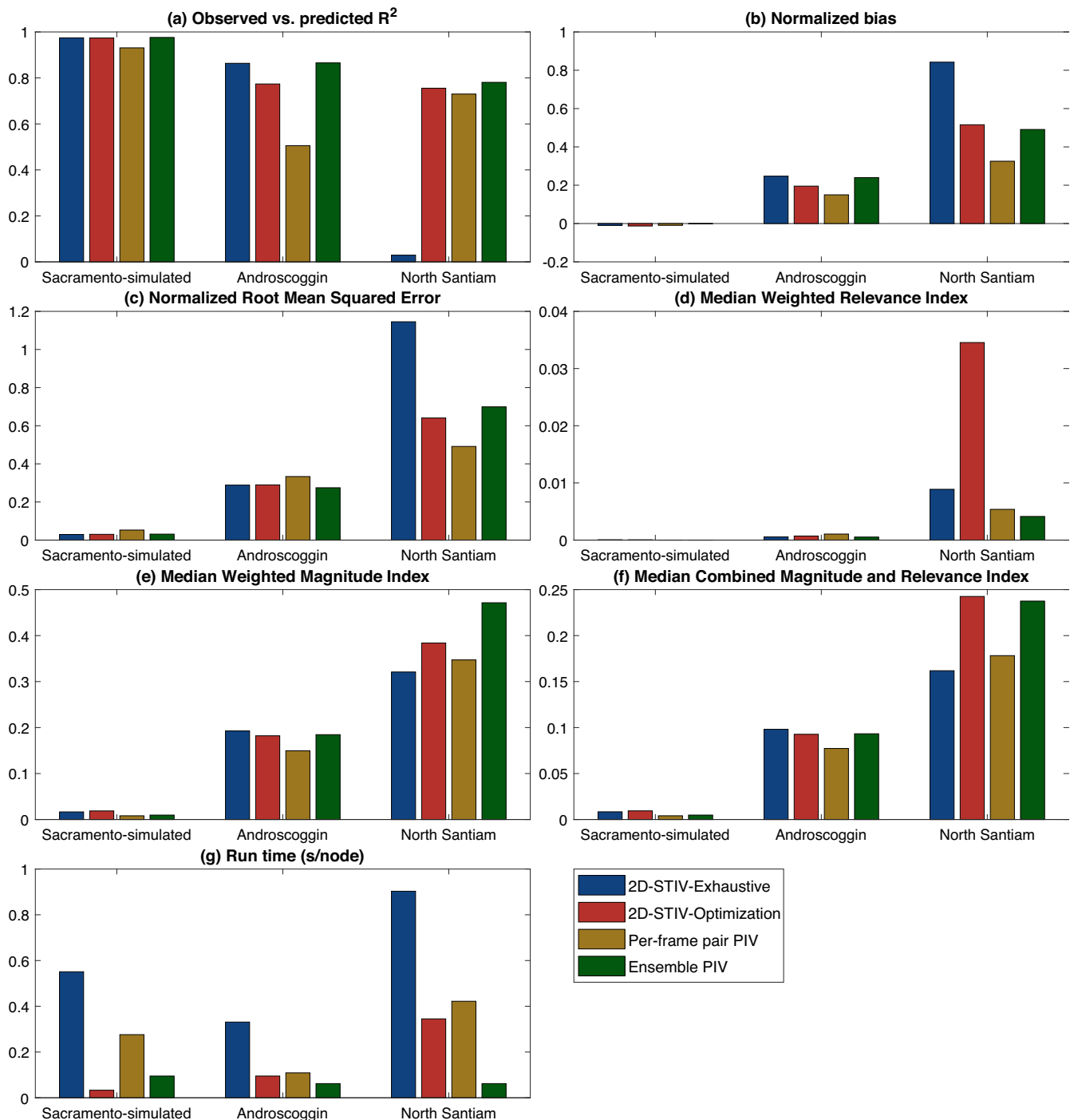


FIGURE 12 Comparison of metrics across the four different image velocimetry algorithms for each site. 2D-STIV, two-dimensional space-time image velocimetry; PIV, particle image velocimetry. [Color figure can be viewed at wileyonlinelibrary.com]

algorithms. Here, we begin by providing some guidance for collecting data suitable for 2D-STIV and for parameterizing the algorithm appropriately. We then contrast the advantages and disadvantages of 2D-STIV and PIV relative to one another and discuss how these algorithms might help advance river image velocimetry.

4.1 | Guidance for data collection and 2D-STIV parameterization

Like any algorithm, effective use of the 2D-STIV workflow requires both careful planning prior to data collection and thoughtful

parameterization of the algorithm. More specifically, given the range of velocities present in the river of interest, one must select a pixel size and image capture interval (i.e., frame rate) that will allow for reliable characterization of the flow field via remote sensing. To help potential users of these algorithms develop some intuition for how to acquire and then analyse image time series for velocity mapping, we focus on three key variables: the size of the pixels making up an image, the rate at which the images are captured, and the velocity of the flow itself. The latter is imposed for a given channel, so our objective herein is to provide guidance for selecting a pixel size and capture interval likely to yield velocity estimates that are accurate and as precise as possible. A theoretical result from Fujita et al. (2019) is useful

TABLE 2 Summary of image velocimetry results for all 12 combinations of site and algorithm.

Site	Algorithm	Obs. vs. pred. R^2	Norm. bias	Norm. RMSE	WRI ₅₀	WMI ₅₀	CMRI ₅₀	Run time (s/node)
Sacramento (simulated)	2D-STIV exhaustive	0.974	-0.010	0.030	0.0001	0.0166	0.0084	0.551
	2D-STIV optimization	0.974	-0.013	0.030	0.0001	0.0187	0.0094	0.033
	Per-frame pair PIV	0.931	-0.009	0.053	0	0.0081	0.0041	0.276
	Ensemble PIV	0.976	-0.002	0.031	0	0.0097	0.0048	0.095
Androscoggin	2D-STIV exhaustive	0.864	0.247	0.289	0.0006	0.1927	0.0981	0.331
	2D-STIV optimization	0.774	0.195	0.290	0.0007	0.1821	0.0927	0.095
	Per-frame pair PIV	0.505	0.150	0.333	0.0011	0.1494	0.0773	0.109
	Ensemble PIV	0.866	0.240	0.275	0.0005	0.1846	0.0933	0.062
North Santiam	2D-STIV exhaustive	0.029	0.842	1.146	0.0089	0.3209	0.1618	0.903
	2D-STIV optimization	0.755	0.516	0.641	0.0345	0.3839	0.2426	0.345
	Per-frame pair PIV	0.730	0.325	0.491	0.0054	0.3472	0.1782	0.422
	Ensemble PIV	0.781	0.491	0.699	0.0041	0.4714	0.2375	0.062

Abbreviations: 2D-STIV, two-dimensional space-time image velocimetry; CMRI₅₀, median combined magnitude and relevance index; Norm., normalized; Obs., observed; PIV, particle image velocimetry; Pred., predicted; WMI₅₀, median weighted magnitude index; WRI₅₀, median weighted relevance index.

in this context: the velocity estimation error is minimized when the streak lines on an STI have an angle θ of 45° . This angle corresponds to a 'rise' of 1 and a 'run' of 1 on an STI, such that $\tan(\theta) = 1$. In other words, a hypothetical, discrete, single-pixel size particle would move by a distance of 1 pixel in the time period between image frames. We can use this line of thinking to calculate an appropriate capture interval S_t given a velocity U and pixel size S_x . For example, for a typical flow velocity of 1 m/s and a pixel size of 0.05 m, similar to that of our UAS-based videos from the Androscoggin and North Santiam Rivers, the ideal capture interval leading to $\theta = 45^\circ$ would be $S_t = S_x/U = [0.05 \text{ m}]/[1 \text{ m/s}] = 0.05 \text{ s}$, or a frame rate of 20 Hz.

We extend this reasoning to a range of different scenarios in Figure 13, in which idealized single-particle STIs are abstracted as lines and plotted as trajectories with time in frames on the horizontal axis and space (i.e., distance traversed along the search line) in units of pixels on the vertical axis. Each line colour represents a distinct flow velocity and the four panels depict different combinations of pixel size and capture interval. As flow velocity increases from the trivial case of 0 m/s, when the particle is not moving and thus remains at the search line origin over the entire time period, up to 2 m/s, the STI lines become steeper because the particle covers a greater distance (number of pixels) in the same amount of time (number of frames). Also note that as the velocity increases, the search lines for velocities separated by a fixed increment of 0.25 m/s become closer together and the difference in streak angle decreases. For example, the difference in angle between the 0.25 and 0.5 m/s lines is much greater (18.4°) than that between the 1.75 and 2 m/s lines ($<1^\circ$). This analysis illustrates why, for a given combination of S_x and S_t , measurement precision, which is essentially the ability to resolve a given difference in velocity, is greatest for low velocities and deteriorates as the flow becomes faster.

However, comparison of Figure 13a and b indicates that precision can be enhanced by reducing the capture interval, which is equivalent to increasing the frame rate. If U and S_x are held constant, halving S_t from 0.2 s in Figure 13a to 0.1 s in Figure 13b, causes each of the STI lines to 'lay down', thus reducing θ for a given U such that the ideal streak angle of 45° corresponds to a velocity of 0.5 m/s rather than 0.25 m/s. Also note that the separation between lines

representing 0.25 m/s intervals of U is greater in Figure 13b than in Figure 13a, indicating that the precision of velocity estimates is greater for the smaller capture interval. If we were to instead increase S_x from 0.05 to 0.1 m while holding S_t constant at 0.2 s (comparing Figure 13a and c), the STI lines would also lay down and reduce θ for a given U . Because halving the capture interval and doubling the pixel size have the same net effect on the STI lines, Figure 13b and c are identical. If we were to both halve S_t and double S_x relative to the base case represented in Figure 13a, we would arrive at Figure 13d, in which the STI lines lay down even more, such that the ideal streak angle of 45° corresponds to a velocity of 1 m/s and the ability to resolve differences in velocity magnitude on the order of 0.25 m/s is further enhanced.

For airborne image acquisition, particularly via UAS, where the flying height and thus pixel size can be easily adjusted, calculations of this kind can help direct flight planning. Typical video cameras are capable of frame rates of 24–30 Hz, so the capture interval can be modified by skipping frames to obtain a value of S_t that will lead to STI streak angles near 45° , given the image pixel size S_x , for the majority of the velocities present in the channel of interest. The trade-offs involved in adjusting either S_x or S_t while holding the other fixed are illustrated in Figure 14 for a constant representative flow velocity of 1 m/s. In the first panel, the pixel size is fixed at 0.05 m while the capture interval varies from 0.05 to 0.5 s in increments of 0.05 s, corresponding to frame rates from 20 to 2 Hz and represented by different coloured lines. Increasing the capture interval (i.e., reducing the frame rate) makes the STI lines 'stand up' straighter as θ increases. For the shortest capture interval of 0.05 s, $S_x = S_t$ and the ideal θ of 45° is achieved, but as S_t increases, the STI lines in Figure 14a become closer together and measurement precision deteriorates. This analysis highlights the importance of capturing image sequences at a sufficiently high frame rate to enable small differences in velocity to be resolved. The second panel in Figure 14 illustrates the effect of varying pixel size while holding the capture interval constant at 0.1 s, also for a fixed U of 1 m/s. As S_x increases from 0.05 to 0.5 m, the STI lines lay down as θ decreases, passing through the ideal 45° for $S_x = 0.1 \text{ m}$. In this case, the separation between STI lines representing S_x increments of 0.05 m decreases as S_x increases, indicating that

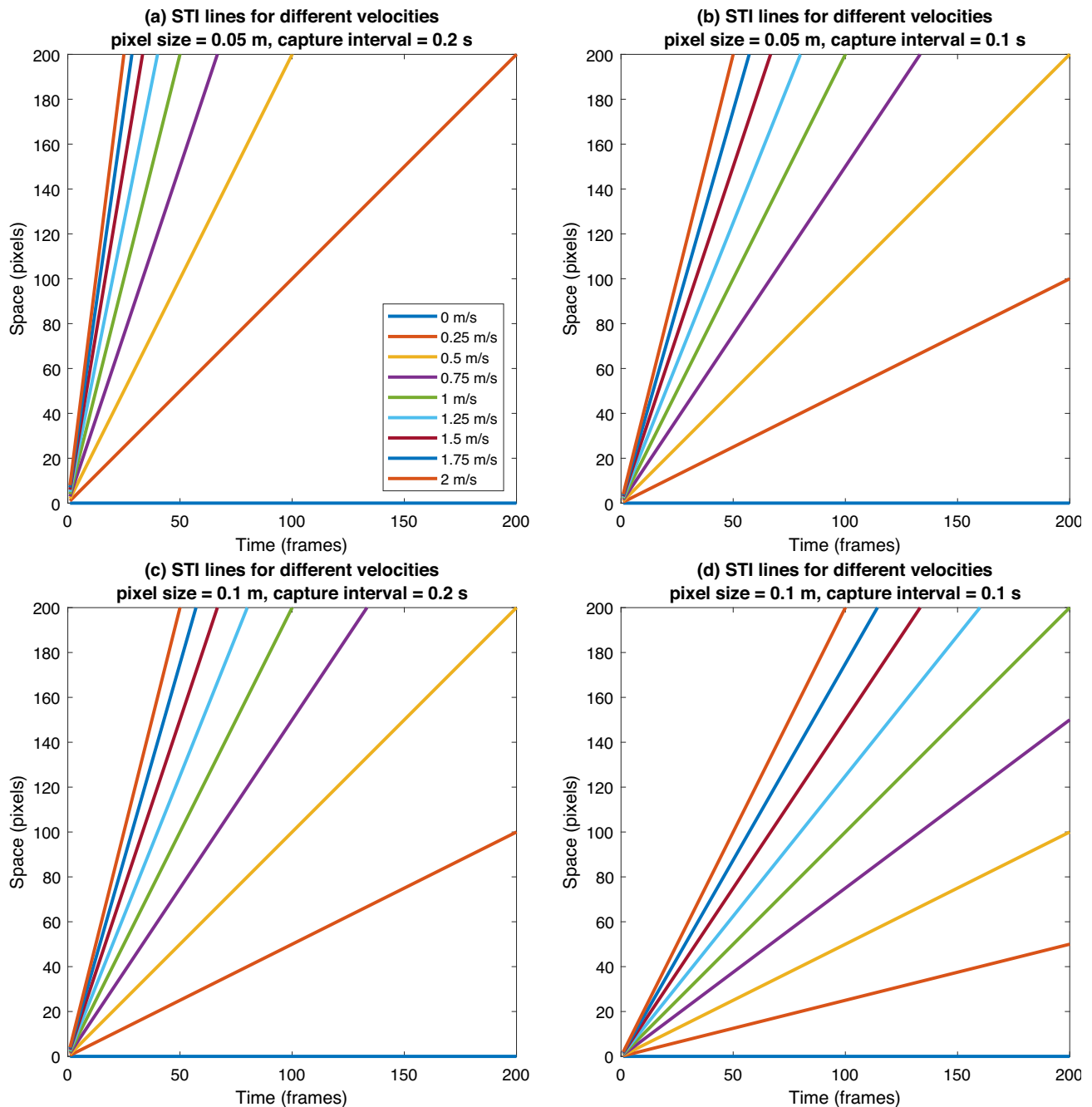


FIGURE 13 Space-time image (STI) lines for different flow velocities and various combinations of pixel size and capture interval. [Color figure can be viewed at wileyonlinelibrary.com]

measurement precision is degraded for coarser pixel sizes. This thought exercise points to the need to acquire images with sufficiently small pixels to distinguish among similar velocities via STIV. Although this paper focuses on the new 2D-STIV algorithm, the preceding discussion pertains to any application of STIV, including the original one-dimensional formulation.

4.2 | 2D-STIV, PIV and potential advances in image velocimetry

As summarized briefly in Section 1, image-based algorithms for estimating flow velocities are increasingly used by researchers and managers across the river community. This growth continues to be fostered by the development of new algorithms and the incorporation

of these algorithms into accessible software tools. In this study, we contributed to this trend by building upon the work of Han et al. (2021) to introduce a new, two-dimensional extension of the popular STIV framework first described by Fujita et al. (2007). We presented two different versions of the 2D-STIV algorithm and compared their output to that from two different variants of PIV. Based on our application of these algorithms to three different test data sets, we can make some tentative statements regarding the relative strengths and weaknesses of 2D-STIV and PIV that could help potential users select an algorithm appropriate for the problem at hand.

The results of this study suggest that the 2D-STIV and PIV algorithms produce similar levels of agreement between the velocities derived from images and those predicted by the hydrodynamic model or measured in the field (Figure 12). An important distinction between 2D-STIV and PIV is that the former requires a higher frame rate and

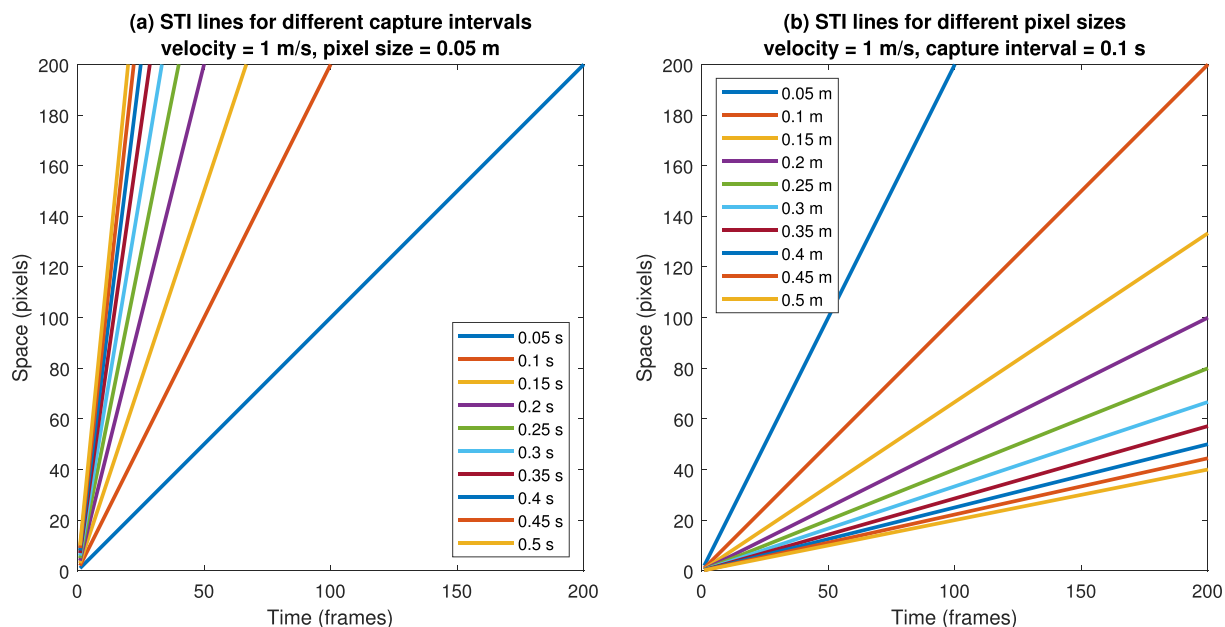


FIGURE 14 Space-time image (STI) lines for (a) a fixed velocity and pixel size but varying capture intervals and (b) a fixed velocity and capture interval but different pixel sizes. [Color figure can be viewed at wileyonlinelibrary.com]

thus a larger number of frames to support an image velocimetry analysis. To infer velocities via STIV, the flow field must be imaged for a sufficient dwell time to create an STI that consists of at least as many frames as the number of pixels along the specified search line. Even longer dwell times are beneficial because calculating the autocorrelation function involves averaging over all possible combinations of frames that are offset from one another by a given time lag (Equation 1). As a result, 2D-STIV tends to require larger data storage volumes, greater computational power, and longer run times than PIV, particularly for the exhaustive version of the 2D-STIV algorithm. The optimization-based implementation can be faster but is also more susceptible to spurious estimates of flow direction. A major advantage of PIV, in contrast, is the ability to infer velocities from a single pair of images. This approach is the basis for the per-frame pair PIV algorithm and the reason why per-frame pair PIV can be used to characterize turbulence and nonstationary flow conditions. The ensemble version of PIV can also be applied to as few as two images but doing so would make the ensemble implementation equivalent to per-frame pair PIV and undercut the enhanced signal-to-noise that can be gained by ensembling over longer time periods.

Our results also suggest that PIV might be more robust than 2D-STIV in terms of the ability to provide smoothly varying velocity estimates throughout a region of interest. Whereas both PIV algorithms produced coherent velocity fields for all three test data sets, the 2D-STIV output for the Androscoggin and North Santiam Rivers included areas with much patchier, more irregular velocity estimates (Figures 8 and 10). Of course, PIV can also be subject to noise, particularly if trackable feature are sparse, but our findings indicate that PIV is less likely to be locally noisy than the new 2D-STIV algorithm. Although we were initially motivated to explore STIV as a means of overcoming the presumed dependence of PIV on discrete particles that could better exploit more diffuse image textures, our results suggest that 2D-STIV might actually be more contingent upon the presence of distinct features than PIV. This inference is based on the observation that the 2D-STIV algorithm performed best for the simulated data set

consisting of simple, spherical particles that were discrete, uniformly distributed, and stationary over time. In this idealized scenario, 2D-STIV performed as well as or better than PIV, but as conditions became more realistic, and thus more challenging, the former algorithm became less reliable. One factor that might have limited the performance of 2D-STIV was the relatively short, 50-pixel search lines we used in this study. Multi-pass PIV is well-equipped to capture structures across a range of scales because the IAs over which correlations are calculated become progressively smaller from one pass to the next, with the initial larger-IA passes essentially serving to ‘hot start’ subsequent passes with smaller IAs. For 2D-STIV, in contrast, the entire pattern of brightness variation from which a velocity is inferred must be observed along a single search line of length n_p , which could limit detection of larger-scale flow features. More specifically, for a natural river with obvious features to track, the foam and froth conveniently available on the Androscoggin, the exhaustive 2D-STIV algorithm was comparable to ensemble PIV overall but patchier locally. For the most complex case of a natural river lacking such clear features, the North Santiam, comparison with ADCP data indicated that the exhaustive 2D-STIV algorithm was essentially uninformative and that the optimization-based version was less reliable than either of the PIV algorithms. These results suggest that 2D-STIV might not be well-suited to the common situation where velocity inference must be made on the basis of subtly advecting patterns of water surface reflectance associated with waves and sun glint; seeding the flow with artificial tracers could lead to more consistent, reliable velocity estimates.

The results of this initial study suggest that the new 2D-STIV algorithm we developed is a viable alternative to well-established PIV-based workflows with a level of performance comparable to existing algorithms. However, further testing across a broader range of river conditions is needed to more fully evaluate the potential and limitations of 2D-STIV. One plausible outcome that could emerge from such investigations might be that STIV is most appropriate for the one-dimensional, single cross-section use case for which the algorithm

was initially developed and continues to be applied in practice. This finding would support the use of STIV for cross section-based discharge measurements, because the velocity estimates produced by STIV represent a spatially and temporally averaged quantity that might be more directly comparable to conventional streamgaging techniques such as ADCPs.

To most effectively apply image velocimetry, broadly defined, the best approach might be to provide end users with a suite of algorithms that can be tested on a case-by-case basis to identify an algorithm that is well-suited to the river of interest and the flow conditions at the time of data collection. Currently, we lack sufficient case studies to know *a priori* which algorithm will perform best for a particular set of circumstances. Until more general insight is gained, integrating existing and yet-to-be-developed tools into a common software ecosystem could allow users to easily evaluate several options. This strategy has proven useful in the context of hydrodynamic modelling, with packages like the International River Interface Cooperative (iRIC, Nelson et al., 2016) providing a germane precedent for advancing the use of image velocimetry in river science and management. Deep learning approaches (e.g., Ansari et al., 2023) could also be considered as such efforts proceed.

5 | CONCLUSION

This study contributed to the growing number of algorithms for inferring flow velocities in river channels from image time series by introducing a two-dimensional, reach-scale implementation of STIV. The workflow outlined herein involves setting up a grid within the channel and then specifying a local, initial guess of the primary flow direction using the centreline tangent vector at each grid node. For a given node, STIs are then extracted from the image sequence along rays radiating from a common origin in a range of candidate flow directions. The advection of water surface features is expressed in these STIs as streak lines, with the angle of these streaks in the (time, space) plane related to the flow velocity. We characterize these streaks by calculating the autocorrelation function of each STI, transforming the ACF into polar coordinates, and identifying the angle that yields the strongest correlation, which corresponds to the inclination of the primary streak lines present in the STI. The velocity magnitude is then calculated from this angle, along with the pixel size and capture interval of the image sequence. To infer the orientation of the velocity vector, we repeat the ACF analysis for STIs along a range of directions and select that which yields the greatest velocity magnitude. Two versions of the 2D-STIV algorithm were presented, one that exhaustively evaluates all candidate flow directions within a specified angular tolerance of the initial guess and another that performs this search using a numerical optimization algorithm. Combining the estimates of magnitude and direction for each grid node thus yields a two-dimensional velocity field with vectors spatially distributed throughout the reach.

To evaluate the performance of the new 2D-STIV algorithm, we applied both the exhaustive and optimization-based versions of 2D-STIV to three test data sets: a simulated image sequence in which the motion of synthetic particles is driven by a modelled flow field and UAS-based videos from two natural channels, one with well-defined patterns of foam and froth that presumably could be easily tracked by the image velocimetry algorithms and another that featured only far

more subtle variations in water surface reflectance. For each site, we compared the 2D-STIV output to that from two established PIV-based algorithms, one implemented on a per-frame pair basis and the other using an ensemble correlation algorithm. The performance of each algorithm at each site was quantified by comparing image-derived velocity estimates to known (i.e., predicted by a hydrodynamic model) or directly measured velocities and computing various measures of agreement, including metrics that considered vector orientation as well as magnitude. Our findings lead to the following conclusions:

The new 2D-STIV algorithm extends STIV beyond single cross sections to continuous, reach-scale mapping of complex flow fields in natural channels. Moreover, 2D-STIV provides information on not only the magnitude of velocity vectors but also their orientation. Quantifying the structure of a space-time image via its autocorrelation function is computationally efficient and allows a range of candidate search line directions to be evaluated at each grid node, either exhaustively or via an optimization-based algorithm. The new 2D-STIV algorithm performed as well as or better than PIV for a simulated data set consisting of idealized, spherical particles that were discrete, uniformly distributed, and stationary over time. For a natural channel with well-defined water surface features, velocities inferred via 2D-STIV agreed closely with direct field measurements, particularly for the exhaustive implementation. The velocity fields generated via 2D-STIV were much more patchy and irregular than velocity fields generated via PIV, however, and vectors from the optimization-based version of the algorithm tended to be more erratic in terms of flow direction than those from the exhaustive version. For a river that lacked obvious water surface features, velocity estimates derived using the exhaustive 2D-STIV algorithm were uncorrelated with ADCP data and both versions of the 2D-STIV algorithm led to areas of local noise and irregular flow directions. Considering all three test data sets, the ensemble PIV algorithm emerged as the most robust image velocimetry algorithm, yielding smooth, coherent velocity fields that were strongly correlated with ADCP measurements. The per-frame pair PIV algorithm can provide more detailed information on turbulence and unsteady flow conditions but led to a patchy, less reliable flow field for one of the natural channels we examined and is more computationally demanding than the ensemble algorithm. The new 2D-STIV algorithm is more demanding in terms of image sequence duration, frame rate and computational run time than established PIV implementations. Importantly, any form of STIV requires that the number of image frames exceeds the number of pixels along the search lines, whereas PIV can be used to infer velocities from a single pair of images. Results from these three case studies suggest that the new 2D-STIV algorithm is a viable alternative to established PIV implementations, but further testing is needed to more fully evaluate the potential and limitations of 2D-STIV. Successful application of STIV requires careful data collection and appropriate parameterization of the algorithm, with thoughtful consideration of the effects of pixel size and capture interval on the precision of image-derived velocity estimates for a given set of flow conditions. Because numerous image velocimetry algorithms are now available, an effective strategy might be to provide end users with a suite of tools, all packaged within a common software environment, that can be tested on a case-by-case basis to select an algorithm that is well-suited to the river of interest under the flow conditions observed at the time of image acquisition.

AUTHOR CONTRIBUTIONS

Carl J. Legleiter, Paul J. Kinzel, Frank L. Engel and Gregory Hewitt contributed to conceptualization. Lee R. Harrison contributed to funding acquisition and investigation (e.g., data collection). Carl J. Legleiter, Paul J. Kinzel and Frank L. Engel contributed to methodology. Carl J. Legleiter developed software and wrote the initial draft, and Paul J. Kinzel, Frank L. Engel, Lee R. Harrison and Gregory Hewitt performed reviewing and editing.

ACKNOWLEDGEMENTS

We would like to acknowledge the NOAA UAS Program Office for supporting this research. Brandon Overstreet, James White, Joshua Price, Max Schwid, Matt Pickett and Brian Taggart assisted with field and UAS data collection on the North Santiam River. Any use of trade, firm or product names is for descriptive purposes only and does not imply endorsement by the US Government.

DATA AVAILABILITY STATEMENT

The video and field measurements of flow velocity from the Androscoggin River are provided in a data release publicly available at <https://doi.org/10.5066/P9H2MM1M>. The field measurements from the Sacramento River and example code for implementing the Simulating Hydraulics and Images for Velocimetry Evaluation and Refinement (SHIVER) framework are compiled in another data release, also publicly available at <https://doi.org/10.5066/P9C19Z0S>. The video and field measurements from the North Santiam River are included in another data release that is publicly available at <https://doi.org/10.5066/P91CX553>.

ORCID

Carl J. Legleiter  <https://orcid.org/0000-0003-0940-8013>

Paul J. Kinzel  <https://orcid.org/0000-0002-6076-9730>

Frank L. Engel  <https://orcid.org/0000-0002-4253-2625>

Lee R. Harrison  <https://orcid.org/0000-0002-5219-9280>

REFERENCES

- Alongi, F., Pumo, D., Nasello, C., Nizza, S., Ciruolo, G. & Noto, L.V. (2023) An automatic ANN-based procedure for detecting optimal image sequences supporting LS-PIV applications for rivers monitoring. *Journal of Hydrology*, 626, 130233. Available from: <https://doi.org/10.1016/j.jhydrol.2023.130233>
- Ansari, S., Rennie, C.D., Jamieson, E.C., Seidou, O. & Clark, S.P. (2023) RivQNet: deep learning based river discharge estimation using close-range water surface imagery. *Water Resources Research*, 59(2), e2021WR031841. Available from: <https://doi.org/10.1029/2021WR031841>
- Biggs, H., Smart, G., Doyle, M., Eickelberg, N., Aberle, J., Randall, M. & Detert, M. (2023) Surface velocity to depth-averaged velocity: a review of methods to estimate alpha and remaining challenges. *Water*, 15(21), 3711. Available from: <https://doi.org/10.3390/w15213711>
- Biggs, H.J., Smith, B., Detert, M. & Sutton, H. (2022) Surface image velocimetry: Aerial tracer particle distribution system and techniques for reducing environmental noise with coloured tracer particles. *River Research and Applications*, 38(6), 1192–1198. Available from: <https://doi.org/10.1002/rra.3973>
- Bodart, G., Le Coz, J., Jodeau, M. & Hauet, A. (2022) Synthetic river flow videos for evaluating image-based velocimetry methods. *Water Resources Research*, 58(12), e2022WR032251. Available from: <https://doi.org/10.1029/2022WR032251>
- Carbonneau, P., Fonstad, M.A., Marcus, W.A. & Dugdale, S.J. (2012) Making riverscapes real. *Geomorphology*, 137(1), 74–86. Available from: <https://doi.org/10.1016/j.geomorph.2010.09.030>
- Conaway, J.S., Eggleston, J., Legleiter, C.J., Jones, J.W., Kinzel, P.J. & Fulton, J.W. (2019) Remote sensing of river flow in Alaska new technology to improve safety and expand coverage of USGS streamgaging. *U.S. Geological Survey Fact Sheet*, 2019(3024), 4. Available from: <https://doi.org/10.3133/fs20193024>
- Dal Sasso, S.F., Pizarro, A. & Manfreda, S. (2021) Recent advancements and perspectives in UAS-based image velocimetry. *Drones*, 5(3), 81. Available from: <https://doi.org/10.3390/drones5030081>
- Dal Sasso, S.F., Pizarro, A., Samela, C., Mita, L. & Manfreda, S. (2018) Exploring the optimal experimental setup for surface flow velocity measurements using PTV. *Environmental Monitoring and Assessment*, 190(8), 460. Available from: <https://doi.org/10.1007/s10661-018-6848-3>
- Duan, J.G., Engel, F.L. & Cadogan, A. (2023) Discharge estimation using video recordings from small unoccupied aircraft systems. *Journal of Hydraulic Engineering*, 149(11), 4023048. Available from: <https://doi.org/10.1061/JHEND8.HYENG-13591>
- Eltner, A., Bertalan, L., Grundmann, J., Perks, M.T. & Lotsari, E. (2021) Hydro-morphological mapping of river reaches using videos captured with UAS. *Earth Surface Processes and Landforms*, 46(14), 2773–2787. Available from: <https://doi.org/10.1002/esp.5205>
- Eltner, A., Sardemann, H. & Grundmann, J. (2020) Technical note: flow velocity and discharge measurement in rivers using terrestrial and unmanned-aerial-vehicle imagery. *Hydrology and Earth System Sciences*, 24(3), 1429–1445. Available from: <https://doi.org/10.5194/hess-24-1429-2020>
- Engel, F.L., Cadogan, A. & Duan, J.G. (2022) Small unoccupied aircraft system imagery and associated data used for discharge measurement at eight locations across the United States in 2019 and 2020. U.S. Geological Survey data release, Available from: <https://doi.org/10.5066/P9H2MM1M>
- Fujita, I. & Hino, T. (2003) Unseeded and seeded PIV measurements of river flows videotaped from a helicopter. *Journal of Visualization*, 6(3), 245–252. Available from: <https://doi.org/10.1007/BF03181465>
- Fujita, I., Notoya, Y., Tani, K. & Tateguchi, S. (2019) Efficient and accurate estimation of water surface velocity in STIV. *Environmental Fluid Mechanics*, 19(5), 1363–1378. Available from: <https://doi.org/10.1007/s10652-018-9651-3>
- Fujita, I., Shibano, T. & Tani, K. (2020) Application of masked two-dimensional Fourier spectra for improving the accuracy of STIV-based river surface flow velocity measurements. *Measurement Science and Technology*, 31(9), 094015. Available from: <https://doi.org/10.1088/1361-6501/ab808a>
- Fujita, I., Watanabe, H. & Tsubaki, R. (2007) Development of a non-intrusive and efficient flow monitoring technique: the space-time image velocimetry (STIV). *International Journal of River Basin Management*, 5(2), 105–114. Available from: <https://doi.org/10.1080/15715124.2007.9635310>
- Han, X., Chen, K., Zhong, Q., Chen, Q., Wang, F. & Li, D. (2021) Two-dimensional space-time image velocimetry for surface flow field of mountain rivers based on UAV video. *Frontiers in Earth Science*, 9, 686636. Available from: <https://doi.org/10.3389/feart.2021.686636>
- Hutley, N.R., Beecroft, R., Wagenaar, D., Soutar, J., Edwards, B., Deering, N., Grinham, A. & Albert, S. (2023) Adaptively monitoring streamflow using a stereo computer vision system. *Hydrology and Earth System Sciences*, 27(10), 2051–2073. Available from: <https://doi.org/10.5194/hess-27-2051-2023>
- Jolley, M.J., Russell, A.J., Quinn, P.F. & Perks, M.T. (2021) Considerations when applying large-scale PIV and PTV for determining river flow velocity. *Frontiers in Water*, 3(December), 151. Available from: <https://doi.org/10.3389/frwa.2021.709269>
- Krynkin, A., Horoshenkov, K.V., Nichols, A. & Tait, S.J. (2014) A non-invasive acoustical method to measure the mean roughness height of the free surface of a turbulent shallow water flow. *Review of Scientific Instruments*, 85(11), 114902. Available from: <https://doi.org/10.1063/1.4901932>

- Legleiter, C.J. & Harrison, L.R. (2023) Video acquired from an uncrewed aerial system (UAS) and hydroacoustic measurements of flow velocity obtained along the North Santiam River, Oregon, in July 2022. U.S. Geological Survey data release, Available from: <https://doi.org/10.5066/P91CX553>
- Legleiter, C.J. & Kinzel, P.J. (2020) Inferring surface flow velocities in sediment-laden Alaskan rivers from optical image sequences acquired from a helicopter. *Remote Sensing*, 12(8), 1282. Available from: <https://doi.org/10.3390/rs12081282>
- Legleiter, C.J. & Kinzel, P.J. (2021) Surface flow velocities from space: particle image velocimetry of satellite video of a large, sediment-laden river. *Frontiers in Water*, 3, 652213. Available from: <https://doi.org/10.3389/frwa.2021.652213>
- Legleiter, C. & Kinzel, P.J. (2023a) Hydrodynamic model output and image simulation code for evaluating image-based river velocimetry from a case study on the Sacramento River near Glenn, California. U.S. Geological Survey data release, Available from: <https://doi.org/10.5066/P9C19Z0S>
- Legleiter, C.J. & Kinzel, P.J. (2023b) The toolbox for river velocimetry using images from aircraft (TRiVIA). *River Research and Applications*, 39(8), 1457–1468. Available from: <https://doi.org/10.1002/rra.4147>
- Legleiter, C.J. & Kinzel, P.J. (2024) A framework to facilitate development and testing of image-based river velocimetry algorithms. *Earth Surface Processes and Landforms*, 49(4), 1361–1382. Available from: <https://doi.org/10.1002/esp.5772>
- Legleiter, C.J., Kinzel, P.J., Laker, M. & Conaway, J.S. (2023) Moving aircraft river velocimetry (MARV): framework and proof-of-concept on the Tanana River. *Water Resources Research*, 59(2), e2022WR033822. Available from: <https://doi.org/10.1029/2022WR033822>
- Legleiter, C.J. & Kyriakidis, P.C. (2006) Forward and inverse transformations between Cartesian and channel-fitted coordinate systems for meandering rivers. *Mathematical Geology*, 38(8), 927–958.
- Ljubičić, R., Dal Sasso, S.F. & Zindović, B. (2024) SSIMS-Flow: image velocimetry workbook for open-channel flow rate estimation. *Environmental Modelling & Software*, 173, 105938. Available from: <https://doi.org/10.1016/j.envsoft.2023.105938>
- Marcus, W.A. & Fonstad, M.A. (2010) Remote sensing of rivers: the emergence of a subdiscipline in the river sciences. *Earth Surface Processes and Landforms*, 35(15), 1867–1872. Available from: <https://doi.org/10.1002/esp.2094>
- MathWorks (2024) MATLAB. Available from: <https://www.mathworks.com/products/matlab.html>
- Mendes, L., Bernardino, A. & Ferreira, R. M.L. (2020) PIV-image-generator: an image generating software package for planar PIV and optical flow benchmarking. *SoftwareX*, 12, 100537. Available from: <https://doi.org/10.1016/j.softx.2020.100537>
- Muste, M., Fujita, I. & Hauet, A. (2008) Large-scale particle image velocimetry for measurements in riverine environments. *Water Resources Research*, 44(WOOD19). Available from: <https://doi.org/10.1029/2008WR006950>
- Nelson, J.M., Shimizu, Y., Abe, T., Asahi, K., Gamou, M., Inoue, T., Iwasaki, T., Kakinuma, T., Kawamura, S., Kimura, I., Kyuka, T., McDonald, R.R., Nabi, M., Nakatsugawa, M., Simoes, F.R., Takebayashi, H. & Watanabe, Y. (2016) The international river interface cooperative: public domain flow and morphodynamics software for education and applications. *Advances in Water Resources* 93(Part A): 62–74. Available from: <https://doi.org/10.1016/j.advwatres.2015.09.017>
- Parsons, D.R., Jackson, P.R., Czuba, J.A., Engel, F.L., Rhoads, B.L., Oberg, K.A., Best, J.L., Mueller, D.S., Johnson, K.K. & Riley, J.D. (2013) Velocity mapping toolbox (VMT): a processing and visualization suite for moving-vessel ADCP measurements. *Earth Surface Processes and Landforms*, 38(11), 1244–1260. Available from: <https://doi.org/10.1002/esp.3367>
- Patalano, A., Garcia, C.M. & Rodriguez, A. (2017) Rectification of Image Velocity Results (RIVER): a simple and user-friendly toolbox for large scale water surface particle image velocimetry (PIV) and particle tracking velocimetry (PTV). *Computers & Geosciences*, 109, 323–330. Available from: <https://doi.org/10.1016/j.cageo.2017.07.009>
- Peña-Haro, S., Carrel, M., Lüthi, B., Hansen, I. & Lukes, R. (2021) Robust image-based streamflow measurements for real-time continuous monitoring. *Frontiers in Water*, 3, 766918. Available from: <https://doi.org/10.3389/frwa.2021.766918>
- Perks, M.T. (2020) KLT-IV v1.0: image velocimetry software for use with fixed and mobile platforms. *Geoscientific Model Development*, 13(12), 6111–6130. Available from: <https://doi.org/10.5194/gmd-13-6111-2020>
- Piégay, H., Arnaud, F., Belletti, B., Bertrand, M., Bizzi, S., Carbonneau, P., Dufour, S., Liébault, F., Ruiz Villanueva, V. & Slater, L. (2020) Remotely sensed rivers in the Anthropocene: state of the art and prospects. *Earth Surface Processes and Landforms*, 45(1), 157–188. Available from: <https://doi.org/10.1002/esp.4787>
- Pumo, D., Alongi, F., Ciraolo, G. & Noto, L.V. (2021) Optical methods for river monitoring: a simulation-based approach to explore optimal experimental setup for LSPIV. *Water*, 13(3), 247. Available from: <https://doi.org/10.3390/w13030247>
- Python.org (2024) Welcome to Python.org. Available from: <https://www.python.org/>
- Randall, M. (2021) Part 11: application of surface velocity methods for velocity and open channel discharge measurements NI GL 100.11–2021, Australian Government Bureau of Meteorology Available from: http://www.bom.gov.au/water/standards/documents/NI_GL_100.11-2021.pdf
- Schweitzer, S.A. & Cowen, E.A. (2021) Instantaneous river-wide water surface velocity field measurements at centimeter scales using infrared quantitative image velocimetry. *Water Resources Research*, 57(8), e2020WR029279. Available from: <https://doi.org/10.1029/2020WR029279>
- Strelnikova, D., Paulus, G., Käfer, S., Anders, K.-H., Mayr, P., Mader, H., Scherling, U. & Schneeberger, R. (2020) Drone-based optical measurements of heterogeneous surface velocity fields around fish passages at hydropower dams. *Remote Sensing*, 12(3), 384. Available from: <https://doi.org/10.3390/rs12030384>
- Strelnikova, D., Perks, M.T., Dal Sasso, S.F. & Pizarro, A. (2023) River flow monitoring with unmanned aerial system. In: Manfreda, S., Ben Dor, E. (Eds.) *Unmanned aerial systems for monitoring soil, vegetation, and riverine environments*. Earth Observation, Elsevier, 231–269. Available from: <https://doi.org/10.1016/B978-0-323-85283-8.00012-6>
- Tauro, F., Tosi, F., Mattoccia, S., Toth, E., Piscopia, R. & Grimaldi, S. (2018) Optical tracking velocimetry (OTV): leveraging optical flow and trajectory-based filtering for surface streamflow observations. *Remote Sensing*, 10(12), 2010. Available from: <https://doi.org/10.3390/rs10122010>
- Thielicke, W. & Sonntag, R. (2021) Particle image velocimetry for MATLAB: accuracy and enhanced algorithms in PIVlab. *Journal of Open Research Software*, 9(1), 12. Available from: <https://doi.org/10.5334/jors.334>
- Watanabe, K., Fujita, I., Iguchi, M. & Hasegawa, M. (2021) Improving accuracy and robustness of space-time image velocimetry (STIV) with deep learning. *Water*, 13(15), 2079. Available from: <https://doi.org/10.3390/w13152079>
- Willman, C., Scott, B., Stone, R. & Richardson, D. (2020) Quantitative metrics for comparison of in-cylinder velocity fields using particle image velocimetry. *Experiments in Fluids*, 61, 62. Available from: <https://doi.org/10.1007/s00348-020-2897-9>

How to cite this article: Legleiter, C.J., Kinzel, P.J., Engel, F.L., Harrison, L.R. & Hewitt, G. (2024) A two-dimensional, reach-scale implementation of space-time image velocimetry (STIV) and comparison to particle image velocimetry (PIV). *Earth Surface Processes and Landforms*, 49(10), 3093–3114. Available from: <https://doi.org/10.1002/esp.5878>